

1 State-dependent network interactions differentially gate sensory input
2 at the motor and command neuron level in *Caenorhabditis elegans*

3

4 Zachary T. Cecere^{1,2,3,†}, Kathleen T. Quach^{1,2,†}, Eviatar Yemini^{4,5}, Javier J. How^{1,2}, Tatyana O.
5 Sharpee^{1,3}, and Sreekanth H. Chalasani^{1,2*}

6 ¹Neurosciences Graduate Program, University of California, San Diego, La Jolla, CA 92093

7 ²Molecular Neurobiology Laboratory, The Salk Institute for Biological Studies, La Jolla, CA 92037

8 ³Computational Neurobiology Laboratory, The Salk Institute for Biological Studies, La Jolla, CA
9 92037

10 ⁴Department of Biological Sciences, Howard Hughes Medical Institute, Columbia University, New
11 York, NY 10027

12 ⁵University of Massachusetts Chan Medical School, Worcester, MA 01655

13 [†]These authors contributed equally.

14 *Corresponding author

15 **Email:** schallasani@salk.edu

16 **Author Contributions:** Z.T.C. designed experiments. Z.T.C. and J.J.H. performed experiments.
17 E.Y. contributed provided strains. Z.T.C. and K.T.Q. analyzed data. K.T.Q., Z.T.C, and S.H.C.
18 wrote the paper. T.O.S. and S.H.C. supervised research.

19 **Competing Interest Statement:** The authors declare no competing interests.

20 **Keywords:** *C. elegans*, whole-brain imaging, network states, sensory gating, soft decision trees

21 **This PDF file includes:**

22 Main Text

23 Figures 1 to 4

24 Supplementary Figures S1 to S8

25 **Abstract**

26 Neural responses are influenced by both external stimuli and internal network states. While
27 network states have been linked to behavioral and stimulus states, little is known about how
28 sensory inputs are filtered by whole-brain activity to affect motor and command neurons. Here,
29 we recorded whole-brain activity of *Caenorhabditis elegans* experiencing bacterial food stimuli,
30 and modeled how sensory inputs affect motor and command neurons in a network state-
31 dependent manner. First, we classified active neurons into six functional clusters: two sensory
32 neuron clusters (ON, OFF), and four motor/command neuron clusters (AVA, RME, SMDD,
33 SMDV). Using encoding models, we found that ON and OFF sensory neurons that respond to
34 onset and removal of bacteria, respectively, employ different adaptation strategies. Next, we used
35 decoding models to show that bacterial onset and removal differentially drive AVA and RME
36 cluster activity. To explore state-dependent effects on AVA and RME clusters, we developed a
37 model that identified network states and fitted submodels for each state to predict how each of
38 the six functional clusters drive AVA and RME cluster activity. We also identified network states in
39 which AVA and RME clusters were either largely unperturbed by or receptive to bacterial sensory
40 input. Furthermore, this model allowed us to disentangle the state-dependent contributions of
41 stimulus timescales and bacterial content to neural activity. Collectively, we present an
42 interpretable approach for modeling network dynamics that goes beyond implication of neurons in
43 particular states, and moves toward explicitly dissecting how neural populations work together to
44 produce state dependence.

45 **Significance Statement**

46 A major function of the brain is to transform sensory information into behavior. As the first
47 receiver of sensory input, sensory neuron activity is often most correlated with stimulus features.
48 However, this high-fidelity representation of sensory input becomes diluted as it travels to
49 downstream neurons, where sensory information is integrated with network activity. By the time
50 sensory information reaches motor neurons, it is often difficult to dissociate the influence of
51 sensory input from the influence of network activity. Here, we describe a method that is fully
52 interpretable such that we can show how neural populations on a whole-brain scale interact to
53 produce network states. From there, we can attribute motor neuron activity to network history and
54 sensory input.

55 56 **Main Text**

57 58 **Introduction**

59
60 Constant stimuli can have variable influences on neural responses and behavior. On the neural
61 population level, this variability becomes more pronounced as sensory information is transformed
62 by downstream neurons. As the initial receiver of sensory information, sensory neurons exhibit
63 activity that is the most correlated with stimulus features, but are susceptible to sensor errors that
64 can propagate to behavior (1, 2). At the perception level, sensory input can be modulated by
65 attention (3, 4), cognitive load (5), perceptual learning (6, 7), internal noise (8, 9), and internally
66 generated coordinated activity (10). At the motor coordination level, gating of sensory input has
67 been observed occurring in phase with behaviors such as locomotion (11, 12) and active
68 whisking (13). However, little is known about how neural populations interact on a global scale to
69 produce network states that modulate how sensory input is gated at the motor neuron level.

70 To disentangle the influences of stimuli and internal network state on downstream neural
71 activity, precise stimulus control and whole-brain imaging are both needed to accurately account
72 for experienced stimuli and global network states. Despite advances in modern imaging
73 technology, most studies are limited to imaging small subsets of a brain's total activity (14–16).
74 This problem is alleviated by studying simpler animals like zebrafish, fly larvae, and adult *C.*
75 *elegans* where neural activity at single-cell resolution can be monitored across the entire brain

76 (17–20). With only 302 neurons, 189 of which are located in the head, the nematode *C. elegans*
77 is ideally suited for whole-brain functional imaging studies. *C. elegans* whole-brain activity can be
78 monitored both in restrained and freely moving animals (20–22). Moreover, whole-brain imaging
79 of restrained animals in a microfluidic chip (20) allows for precise, fast, and complex stimuli
80 presentations, thereby enabling investigations of stimulus-evoked whole-brain global dynamics
81 underlying sensory coding (23, 24), motor states (25), and physiological states (26, 27). While
82 these studies demonstrate the utility of whole-brain imaging and provide insights into the
83 nematode nervous system, modeling of global network activity has largely focused on identifying
84 which neurons and activity trends underlie particular behavioral or sensory states, but often fall
85 short of explaining how populations work together to influence neural activity.

86 Here, we imaged the calcium activity of the entire *C. elegans* head while we presented it
87 with rapidly fluctuating sequences of bacterial food stimuli and control buffer. We chose bacterial
88 food instead of single-compound odorants in order to study a complex stimulus that is
89 immediately relevant to *C. elegans*. We correlated activity of individual neurons to show that
90 active neurons can be divided into six functional clusters groups. We then used encoding and
91 decoding models to characterize basic properties of how stimuli drive sensory neurons and
92 motor/command neurons. Finally, we built a hybrid model to identify network states and build
93 submodels to explicitly show how sensory and motor populations drive motor/command neuron
94 activity in each state. This model allowed us to identify network states in which motor/command
95 neurons were either unresponsive or responsive to sensory input. Furthermore, we revealed how
96 stimulus features and sensory context were differentially gated in a state-dependent fashion.

97 98 **Results**

100 **Food-stimulated whole-brain activity reveals six functional cell clusters**

101 We used an automated microfluidic system (28) to simultaneously image calcium activity in *C.*
102 *elegans* head neurons and present the animal's nose with pulse-based stimulus sequences that
103 rapidly fluctuated between liquid flows of bacterial food stimulus (from channel 1) and control
104 buffer (from channel 2) (Fig. 1A, see Materials and Methods: Stimulus delivery). We refer to this
105 as the bacteria↔buffer stimulus sequence. To control for artifacts intrinsic to the microfluidic
106 setup, we also imaged activity while *C. elegans* was presented with a control buffer↔buffer
107 stimulus sequence that fluctuated between two chemically identical buffer flows. This microfluidic
108 system was previously used to show that individual chemosensory neurons detect and respond to
109 bacteria (29, 30). To monitor whole-brain activity (see Materials and Methods: Whole-brain
110 imaging), we used a strain that expressed a genetically-encoded nuclear-localized calcium
111 indicator (GCaMP5K) (25,31). This strain was previously used to obtain whole-brain activity from
112 restrained *C. elegans* during controlled delivery of stimuli (20, 25). In addition to this primary
113 strain, we also recorded calcium activity (GCaMP6s) (32) from a strain that expressed NeuroPAL
114 (24), which labels all *C. elegans* neurons with an invariant multicolor fluorescence map and
115 allows for unambiguous identification of neurons (Fig. 1B-D). We used this as a supplementary
116 strain to confirm cell identity associated with activity patterns found in the primary strain.

117 We found that active neurons could be divided into six functional clusters based on
118 correlated changes in GCaMP fluorescence: two sensory neuron clusters (ON and OFF) and four
119 motor/command neuron clusters (AVA, RME, SMDD, SMDV) (Fig. 1E–H). We first identified
120 primary sensory neurons by looking for neurons that were either positively correlated (ON cells)
121 or negatively correlated (OFF cells) with bacteria pulse onset during bacteria↔buffer stimulus
122 sequences. Specifically, for each neuron, we first subtracted the changes in fluorescence induced
123 by bacteria removals from the changes in fluorescence induced by bacteria onsets, and then
124 ranked each neuron according to this score (see Materials and Methods: ON and OFF sensory
125 neuron classification). The neurons with the highest and lowest scores were then checked for
126 additional criteria before being classified as ON cells and OFF cells, respectively. ON cells were
127 categorized as those neurons that obviously and immediately increased activity upon all bacteria
128 onsets, and immediately decreased upon bacteria removals (Fig. 1I). Conversely, OFF cells were
129 classified as neurons that decreased activity upon bacteria onsets and increased upon bacteria

130 removals (Fig. 1I). OFF cells were additionally required to rapidly decrease activity in response to
131 initial bacterial onsets, dropping well below their pre-stimulus baseline, indicating that these
132 sensory neurons are inhibited by bacteria rather than activated by the control buffer flow (Fig. 1I).
133 This OFF cell behavior of being inhibited by a stimulus was absent in the control buffer↔buffer
134 stimulus sequences. Instead, we found only ON cells that were activated by either the onset of
135 the channel 1 buffer (ON-1 cells) or the onset of channel 2 buffer (ON-2 cells) (Fig. S1).
136 Additionally, we identified fewer sensory neurons in animals presented with buffer↔buffer
137 stimulus sequences (Fig. S1A) than with bacteria↔buffer stimulus sequences (Fig. 1F,G). This
138 suggests that additional sensory neurons respond during bacteria ↔ buffer stimulus sequences,
139 compared to buffer↔buffer stimulus sequences. Therefore, bacteria↔buffer stimulus sequences
140 activate ON and OFF sensory neurons that respond to bacteria onset and removal, respectively,
141 rather than to bacteria onset and buffer onset.

142 The vast majority of neurons did not respond immediately to stimulus changes (Fig. 1F–
143 H). Across these neurons, we observed two pairs of stereotypical activity patterns: a pair of
144 clusters that were anti-correlated and bistable (Fig. 1H, red and blue), and a pair of clusters that
145 were anti-correlated and moderately fast (Fig. 1H, purple and yellow). Using the NeuroPAL–
146 GCaMP6s strain to identify neurons, we found that RME motor neurons and AVE command
147 neurons were anti-correlated and bistable (Fig. 1J), consistent with previous findings (25). We
148 also found that SMDD and SMDV neurons were anti-correlated and exhibited moderately fast
149 dynamics (Fig. 1K). These 4 representative motor and command neurons are associated with
150 forward locomotion (RME), reverse locomotion (AVA), dorsal turning (SMDD), and ventral turning
151 (SMDV) in *C. elegans* (25, 34–37). Using AVA, RME, SMDD, and SMDV as representative
152 neurons, we sorted non-sensory neurons into clusters based on how their activity correlated with
153 these four representative neurons (Fig. 1I–K). Many of the low noise neuronal traces strongly
154 correlated (>85%) with either the identified RME motor neurons or AVA command neurons (Fig.
155 1F,G). A number of other calcium traces appeared as distorted, noisy versions of AVA or RME
156 (Fig. S2), and the counts shown in the Fig. 1F,G are likely an underestimate of the true number of
157 cells that are highly correlated with AVA and RME. In contrast, SMDV and SMDD were often the
158 sole members of their eponymous clusters, usually with no other neurons that strongly correlated
159 with these neurons (Fig. 1F,G). AVA, and RME were previously shown to have strong positional
160 stereotypy, and thus, after identifying these neurons with NeuroPAL, their activity signature and
161 stereotyped location made them easy to identify in the absence of NeuroPAL. SMDV and SMDD
162 neurons were also readily identified by their previously reported distinctive activity signature (37).
163 Therefore, we were able to subsequently identify all four motor/command neuron clusters in non-
164 NeuroPAL-GCaMP5K animals without a coinciding NeuroPAL map (Fig. 1F,G).

165 These six cell clusters appeared in every animal, and we could not identify any other cell
166 cluster that appeared consistently across all animals exposed to bacteria↔buffer stimulus
167 sequences. We also observed similar clustering of active neurons in animals exposed to
168 buffer↔buffer stimulus sequences (Fig. S1A). Putative cells not appearing in one of the
169 aforementioned six cell clusters typically resembled noise or noisier versions of the activity
170 patterns exhibited by the six cell clusters. To reduce dimensionality of the dataset with little loss of
171 information (due to high correlation), we averaged across the activity traces of all neurons within
172 a cluster (1I–K). Hence, all subsequent modeling used cluster-averaged representations to
173 simplify model structure.

174

175 **Bacteria addition and removal differentially drive activity of sensory, AVA, and RME** 176 **clusters**

177 To analyze how ON and OFF sensory neurons differ in their responses beyond the single-pulse
178 timescale, we built encoding models to predict how sensory neuron activity adapts to repeated
179 stimuli presentations (Fig. 2A, see Materials and Methods: Encoding model). Both ON and OFF
180 cells are driven away from baseline activity (in opposite directions) upon bacteria onset and return
181 to baseline upon bacteria removal. ON and OFF cells habituate to repeated bacteria
182 presentations such that the change (increase for ON, decreases for OFF) in fluorescence from
183 baseline is smaller in subsequent bacteria pulses (Fig. 1I). Here, we explored which timescale of

184 adaptation best described ON and OFF cells: 1) perfect adaptation, in which neurons cease
185 responding despite persistent stimulation, 2) imperfectly adapting adaptation, in which neurons
186 attenuate but do not fully terminate their responses, and 3) non-adaptation, in which neural
187 responses are unaffected by recent stimulus history.

188 To examine the timescales of adaptation in ON and OFF cells, we used a cascade model
189 that was previously used to describe adaptation to odors in *C. elegans* sensory neurons (38).
190 This model is built on a cascade of simple ordinary differential equation (ODE) models of the
191 form:

$$\begin{aligned} dx_i/dt &= \tau * ([input] - x_i(t)) \\ X(t) &= x_1(t) - x_2(t) \end{aligned}$$

193 where τ is the time constant that controls how fast a linear temporal filter responds to stimulus
194 $[input]$. The temporal filter describes how the recent history of the stimulus contributes to the
195 current value of inferred calcium level of the cell, $X(t)$. With τ constrained to be positive, $X(t)$ is
196 guaranteed to exhibit perfect adaptation. That is, when encountering a step-change stimulus,
197 $X(t)$ will briefly change activity before terminating the response and returning to its baseline level.
198 This model performed well for uncorrelated stimulus patterns but struggled considerably on
199 correlated patterns (38). Kato and colleagues supposed these issues could be mediated by
200 including more than two of the simple ODE filters. In other words, the authors hypothesized that
201 *C. elegans* sensory cells adapt at more than one timescale. To test this hypothesis, as well as to
202 ascertain whether the perfect adaptation assumption is justified, we simplified and generalized
203 this model:

$$\begin{aligned} \frac{dx_i}{dt} &= \tau \cdot ([input] - x_i(t)) \\ X(t) &= \sum a_i x_i(t) \\ g(t) &= (x^p \otimes f_g)(t) \end{aligned}$$

205 where $x(t)$ is the inferred calcium level of the cell and is calculated as the sum of the temporal
206 filters (ODE model solutions), f_g is the GCaMP filter, and p is a positive value required for the
207 GCaMP transformation. This model learns the coefficients τ and a_i for an arbitrary number of
208 ODE basis function, and thus can learn adaptation on multiple timescales. Moreover, this model
209 can test the effects of perfect and imperfect adaptation on model fit by toggling the coefficient
210 constraint, such that perfect adaptation entails the following constraint:

$$\sum a_i = 0$$

212 This model formulation produced consistent and robust fits to *C. elegans* sensory
213 neurons and allowed us to test the effects of different model complexities. In this approach, each
214 sensory neuron's fluorescence trace was divided into three contiguous blocks. We used a 3-fold
215 cross validation approach (i.e., two of the blocks are used to fit the model, while the third is used
216 for testing) to assess model performance as a function of the number of basis filters and the type
217 of adaptation. For ON cells, all adapting models significantly outperformed the non-adapting
218 model according to a hierarchical bootstrap ($p < 0.05$ with Bonferroni correction, Fig. 2B, S3A). A
219 perfectly adapting model with one primary filter and one adapting filter performed best, matching
220 previous findings (38). Similarly, OFF cell adapting models outperformed the non-adapting model
221 (Fig. 2C, S3B). However, unlike ON cells, OFF cells were best described by an imperfectly
222 adapting model with one primary filter and one adapting filter, while the perfectly adapting model
223 was the worst-performing model (not significantly better than non-adapting model) (Fig. 2C, S3B).
224 It is possible that OFF sensory cells perfectly adapt over a longer timescale, but the fast
225 adaptation relevant to this study is imperfect in OFF cells. Using more than two basis functions

226 (one primary filter and one adapting filter) hurt cross-validation performance (data not shown).
227 While previous studies hypothesized that more than two cascade equations were required to
228 model adaptation on multiple timescales (38), here we found that the type of adaptation and not
229 the number of cascade equations to be more important for modeling OFF sensory neurons.

230 We also compared the timescales of ON and OFF temporal filters. For both ON cells and
231 OFF cells, primary filters are fast and follow the fluctuation of stimuli, while the adapting filters
232 reflect the slower timescale of adaptation. While ON and OFF cells displayed similar timescales in
233 their primary filters, OFF cells have faster adapting filters (higher τ and lower time-to-half-peak)
234 than ON cells (Fig. 2D,E). Thus, the OFF cell rebound was fast relative to ON cell habituation.
235 Moreover, the OFF cell rebound was weak compared to ON cell habituation. In the best-
236 performing OFF cell model, the adapting filter coefficient was typically smaller in magnitude than
237 the primary filter coefficient (Fig. 2E). Thus, the OFF cell adapting filter does little to temper
238 stimulus inhibition of OFF cells. Instead, it seems to be designed to produce fast rebounds to
239 bacteria removal.

240 Adaptation appears to have different goals in ON and OFF cells. ON cells obey a fairly
241 straightforward perfect adaptation law that can be explained by calcium depletion. OFF cells, on
242 the other hand, exhibit an imperfect, fast rebound strategy. This latter strategy will not efficiently
243 encode stimulus across large concentration scales. It will, however, maintain a higher dynamic
244 range for constrained concentrations scales. We surmise that ON sensory cells may be designed
245 to work across larger concentration scales, engaging specific OFF cells for specific concentration
246 ranges. Overall, we show that ON and OFF sensory neurons have different adaptation kinetics to
247 rapidly fluctuating bacterial stimulus sequences.

248 To determine how different phases of stimulus presentation affects motor neurons, we
249 next built decoding models to predict stimulus state from motor/command cluster activity (see
250 Materials and Methods: Decoding model). In bacteria \leftrightarrow buffer stimulus sequences, bacteria
251 pulses are effectuated by directing bacteria flow from channel 1 over the *C. elegans* nose (Fig.
252 2F), while buffer pulses result when buffer from channel 2 flows over the nose and displaces the
253 bacterial flow (Fig. 2G). Since *C. elegans* is positioned asymmetrically in the microfluidic chip
254 relative to the two channels (channel 1 is slightly closer to the nose), we also analyzed animals
255 presented with buffer \leftrightarrow buffer stimulus sequences to control for mechanosensory responses to
256 differences in flow properties between the two channels (Fig. 2H).

257 Unlike sensory neuron clusters, shifts in motor/command neuron cluster activity do not
258 reliably coincide with stimulus transitions (Fig. 1H–K). Therefore, we used multinomial logistic
259 regression (MLR) to predict the probabilities of a particular stimulus state given motor neuron
260 cluster activity inputs. MLR (39) is a robust classification model that, when combined with class
261 balancing, has a very natural null model: prediction from worm identity only. Here, linear
262 predictions about stimulus state are generated by linearly combining a set of weights with
263 explanatory variables of a given observation:

264

$$P(S_i|X(t)) = \text{softmax}(\sum_{n=1}^k \beta_{i,k} X_k(t))$$

266

267 where $S_i(t)$ is the stimulus class i at time window i . The k -dimensional $X(t)$ captures motor
268 neuron cluster activity at time window t along with worm identity information. $\beta_{i,k}$ is made up of
269 the coefficients for stimulus state i , which are regularized using an L1 norm and learned using
270 gradient ascents. 16-second time windows of motor/command neuron cluster activity data were
271 divided into thirds (5.33 seconds each). To predict the stimulus state in the middle subwindow (t -
272 2.67s to t +2.67s, with t as the halfway point of the prediction window), motor/command neuron
273 cluster activity data from the first subwindow (t -8s to t -2.67s) and the last subwindow (t +2.67s to
274 t +8s) were used for the decoding task (see Materials and Methods: Decoding model).

275 We used this model to decode neural activity inputs from AVA, RME, SMDD, and SMDV
276 clusters (Fig. 2I). Worm identity was also considered to capture variability across animals. The
277 decoding model predicted four stimulus states for bacteria \leftrightarrow buffer stimulus sequences:
278 prolonged bacteria, prolonged buffer, bacteria-to-buffer transition, and buffer-to-bacteria transition

279 (Fig. 2I). Importantly, initial onsets and removals of bacteria are included in transition states, but
280 not in prolonged states. For buffer↔buffer stimulus sequences, corresponding states based on
281 channel activation were predicted. In predicting stimulus states associated with bacteria↔buffer
282 stimulus sequences, decoding from the activity of the RME and AVA cluster pair improved
283 performance over decoding from identity alone in both non-NeuroPAL-GCaMP5K (99.3% of
284 bootstraps, Fig. 2J) and NeuroPAL-GCaMP6s (99.4% of bootstraps, Fig. S4A) strains. In
285 contrast, decoding from the activity of the SMDD and SMDV cluster pair did not perform better
286 than the null model (Fig. S4B). Moreover, RME and AVA cluster activity could also be used to
287 predict stimulus state in buffer↔buffer stimulus sequences, outperforming prediction from worm
288 identity alone (Fig. S4C).

289 The decoding model produced linear temporal filters that described how stimulus states
290 contributed to motor/command neuron cluster activity. Temporal filters for buffer↔buffer stimulus
291 sequences revealed that flow from both buffer channels had similar effects on motor/command
292 cluster activity. Prolonged buffer from either channel was associated with similar transient
293 increases in both AVA and RME cluster activity (Fig. 2K,L). Both types of buffer-to-buffer
294 transitions (channel 1 → channel 2, channel 2 → channel 1) reduced AVA cluster activity while
295 RME cluster activity remained near baseline (Fig. 2M,N). In contrast, temporal filters for
296 bacteria↔buffer stimulus sequences indicated that bacteria and buffer differentially drove AVA
297 and RME cluster activity. Prolonged bacteria was associated with sustained increase in RME
298 cluster activity and strong decrease in AVA cluster activity (Fig. 2O), while prolonged buffer was
299 associated with sustained inhibition of RME cluster activity and low AVA cluster activity (Fig. 2P).
300 The bacteria-to-buffer transition induced a slow increase in RME cluster activity, while AVA
301 cluster activity remained near baseline (Fig. 2Q). The temporal filter predicting bacteria-to-buffer
302 transition from RME cluster activity (Fig. 2Q) resembled a diminished version of the temporal filter
303 predicting prolonged bacteria (Fig. 2O), suggesting that bacteria removal did not immediately
304 alter RME activity. The converse buffer-to-bacteria transition is associated with rapid peak in AVA
305 cluster activity and near-baseline RME cluster activity (Fig. 2R). The temporal filter for predicting
306 buffer-to-bacteria transition from AVA cluster activity (Fig. 2R) is higher in magnitude than the
307 temporal filter predicting prolonged buffer from AVA cluster activity (Fig. 2P), suggesting that
308 bacteria onset has an immediate effect on the AVA cluster. Bacteria↔buffer decoding models
309 were also remarkably similar across non-NeuroPAL-GCaMP5K and NeuroPAL-GCaMP6s
310 strains (Fig. S4D-G). Altogether, these results suggest that bacteria presentation biases the
311 AVA-RME cluster pair towards RME cluster activation (associated with forward locomotion),
312 while bacteria removal biases the cluster pair towards AVA cluster activation (associated with
313 reverse locomotion). Furthermore, motor/command responses to buffer differ depending on
314 whether the overall sensory context also includes bacterial stimuli.

315

316 **Identification of interpretable network states that vary in sensory gating properties**

317 Based on our previous decoding results that AVA and RME motor/command clusters are
318 influenced by sensory input, we next investigated how global network activity and sensory input
319 drive AVA and RME cluster activity under different network states. We created a hierarchical
320 model that used a soft decision tree (SDT) gating model (40) to identify relevant network states,
321 and then we fitted MLR forecasting submodels for each network state to predict AVA and RME
322 cluster activity (see Materials and Methods: SDT-MLR model). This combination of models,
323 which we refer to as the SDT-MLR model, overcomes the limitation of using a single linear model
324 to describe motor neuron cluster activity. For instance, members of the AVA cluster are bistable:
325 they have upper and lower stable states (boundedness). Also, activity in these cells appears to
326 have momentum: when one of these cells begins a transition between its stable states, it will tend
327 to complete that transition. A single, linear model is unable to describe both momentum and
328 boundedness. An appropriate model should learn the positive correlation between future AVA
329 cluster rise and past AVA cluster increases to capture momentum. At the same time, this positive
330 correlation should weaken and become negative as AVA nears its upper bound as these cells do
331 not rise above that limit. Here, we employed multiple MLR models to capture nonlinear dynamics,
332 including features like momentum and boundedness. We then used an SDT gating model to route

333 in recent network activity (AVA, RME, SMDD, SMDV clusters) to different network states. Each of
334 these network states is associated with a different MLR model. In so doing, the SDT parceled the
335 space of network trajectories into subspaces in which network evolution can be approximated by
336 linear, probabilistic models. This parcellation and linearization strategy is similar to what has been
337 previously used (41). In our SDT–MLR modeling, there were $M \times N$ MLR submodels, where M is
338 the number of models being compared and N is the number of states parceled by the SDT. If the
339 stimulus effect depends on network history, then we expect that the stimulus filters will differ
340 across MLR submodels. As an end-to-end interpretable distillation of a neural network, the SDT is
341 capable of learning complex, non-linear features. Moreover, since both the SDT and MLR
342 submodels are differentiable, they can be simultaneously fit using gradient-based optimization
343 methods.

344 We started by comparing forecasting models that predict AVA and RME cluster activity
345 from recent network and sensory neuron activity, with models that predict from network history
346 alone. This allowed us to assess whether sensory input from bacteria↔buffer stimuli were more
347 relevant in some network states compared to others. Using recent network history inputs from
348 AVA, RME, SMDD, and SMDV clusters, the full SDT-MLR model was fitted to a hyperparameter
349 set for predicting RME and AVA calcium change (rise and fall). This model generated a tree with
350 three levels, consisting of top level filters, along with right and left subtree filters (Fig. S5A), and
351 four network states that produced the best results (Fig. 3A, S5B,C, see Materials and Methods:
352 SDT–MLR model). State 1 and 4 were transient states, with state 1 associated with AVA cluster
353 peaks, and state 4 associated with RME cluster peaks (Fig. 3A). In contrast, state 2 and 3 were
354 persistent states (Fig. 3A). State 2 was characterized by high AVA, low RME, low SMDV, and
355 high SMDD cluster activities, while state 3 exhibited the opposite (Fig. 3A). After network states
356 were identified, the SDT was then frozen, and the MLR submodels were fitted to the rest of the
357 data in an out-of-bootstrap cross-validation strategy to assess feature variability (42).

358 In the out-of-bootstrap cross-validation, inclusion of ON and OFF sensory neuron activity
359 improved overall model performance (summed across states) in >95% of bootstraps. However,
360 when considering model performance for individual network states, inclusion of sensory activity
361 was only useful in states 3 and 4, but provided little predictive value in states 1 and 2 (Fig. 3B),
362 despite the variance in stimulus sequence being similar across all states. Both sensory-
363 responsive states (states 3 and 4) are characterized by low AVA and high RME cluster activities,
364 both of which are associated with forward locomotion (Fig. 3B). Conversely, the sensory-
365 unresponsive states (states 1 and 2) display the opposite activity trends with high AVA and low
366 RME cluster activities, which are associated with reverse locomotion (Fig. 3B). This suggests that
367 sensory input is gated more heavily during reverse locomotion than during forward locomotion,
368 and that forward locomotion is a sensory-responsive behavior.

369 For each state, the SDT–MLR model generated linear temporal filters that predicted how
370 recent network history from AVA, RME, SMDV, and SMDD clusters affected the probability of
371 AVA and RME activity trends. In general, temporal filters were similar across predicted neural
372 activity associated with forward locomotion (AVA fall, RME rise; Fig. 3C, middle two rows), as well
373 as across activity associated with reverse locomotion (AVA rise, RME fall; Fig. 3C, top and
374 bottom rows). Additionally, temporal filters were similar across the sensory-unresponsive states
375 (state 1 and 2), except that recent SMDV history had a diminished effect on forward-associated
376 activity in state 2. Linear filters across the sensory-responsive states (state 3 and 4) resembled
377 each other, except for how network history drove AVA fall in state 4. Notably, RME cluster history
378 drove AVA and RME cluster activity in general in sensory-unresponsive states, but had a neutral
379 or suppressive effect in sensory-responsive states. Some state-invariant trends included the
380 suppressive effect of SMDD history on AVA rise, as well as the suppressive effect of AVA on
381 RME rise (Fig. 3C). Here, we describe some of the general trends of how network history
382 influenced AVA and RME cluster activity in a state-dependent fashion, but Fig. 3C can be readily
383 interpreted to understand in detail how each motor/command cluster affected AVA and RME
384 cluster activity in each state.

385 Next, we looked at how sensory input influences particular AVA and RME cluster activity
386 trends under different network states. As expected from Figure 3B, temporal filters predicting AVA

387 and RME cluster activity from ON and OFF sensory activity were generally flat in states 1 and 2,
388 indicating that sensory information was broadly suppressed from motor/command activity in these
389 states (Fig. 3D). In contrast, states 3 and 4 exhibited more temporal filters in which sensory
390 activity either increased or decreased the probability of AVA and RME activity trends (Fig. 3D).
391 The largest effects of sensory input are on reverse-associated motor/command activity (AVA rise,
392 RME fall), which is suppressed by ON activity and elevated by OFF activity (Fig. 3D). Within
393 reverse-associated activity, OFF activity has a greater influence on AVA rise, while ON activity
394 has a greater influence on RME fall (Fig. 3D). Additionally, ON sensory input drives RME rise in
395 state 3 (Fig. 3D), suggesting that forward locomotion that characterizes state 3 can be maintained
396 with ON activation of RME and OFF suppression of AVA. Overall, we show that SDT-MLR
397 models can be used to identify relevant network states, characterize how those states are
398 generated by network history, and delineate the state-dependent effects of stimuli on
399 motor/command neuron activity.

400

401 **Effect of stimulus timescales and sensory context on AVA and RME clusters**

402 To further deconstruct sensory influences on AVA and RME cluster activity, we divided
403 bacteria↔buffer stimulus sequences into stimulus patterns with either low- or high-variance pulse
404 protocols, and fitted separate SDT-MLR models using corresponding neural activity (Fig. S6, S7).
405 The main difference between low- and high-variance protocols is that alternating stimulus blocks
406 consist of a single long pulse in the former, and composed of multiple short pulses in the latter
407 (see Materials and Methods: Division of stimulus sequences). In general, high-variance pulses
408 generally had more effect on AVA and RME cluster activity than low-variance pulses (Fig. 4A). To
409 compare the overall effect of each network state on sensory gating, we summed the absolute
410 values of magnitudes from all temporal filters within a state (Fig. 4A, last row). While high- and
411 low-variance stimulus pulses had similar overall effects in state 4, high-variance pulses had more
412 than twice as much influence as low-variance pulses in state 3 (Fig. 4A, last row). Particularly in
413 state 4, low-variance pulses can result in uneven influence from ON and OFF neurons, such as
414 greater ON influence on RME fall and greater OFF influence on AVA rise (Fig. 4A). While state 1
415 and 2 were initially deemed to be broadly unresponsive to sensory input (Fig. 3B), enriching the
416 model with a subset of pulse lengths revealed some sensory influence in state that was
417 previously masked when all timescales were considered. For example, in state 1, high-variance-
418 pulse ON activity promoted AVA fall, while high-variance-pulse OFF activity suppressed AVA fall
419 (Fig. 4A). These opposite effects likely canceled each other out when all stimulus pulse lengths
420 were considered, thereby resulting in a sensory-unresponsive model prediction (Fig. 3D).
421 Furthermore, segregation of stimuli by low- or high-variance pulses revealed more sensory
422 influence on forward locomotion in states 3 and 4 (Fig. 4A) that was previously undetected in the
423 all-pulse SDT-MLR model (Fig. 3D). Thus, the SDT-MLR model can be used to also detect
424 feature-specific effects of stimuli on motor/command neuron activity.

425 We next explored the ability of SDT-MLR models to differentiate sensory contexts by
426 comparing buffer↔buffer and bacteria↔buffer stimulus sequences. Since high-variance pulses
427 were shown to have greater overall effect (Fig. 4A), we compared only high-variance pulses from
428 buffer↔buffer and bacteria↔buffer stimulus sequences. In the SDT-MLR model for
429 buffer↔buffer stimulus sequences (Fig. S8), inclusion of buffer↔buffer sensory activity improved
430 overall performance only for state 4 (Fig. S8A). Compared to bacteria↔buffer sensory input,
431 temporal filters predicting AVA and RME cluster activity from buffer↔buffer sensory input typically
432 displayed slower timescales (Fig. S8C). Based on the sum of absolute magnitudes of all temporal
433 filters within a state, buffer↔buffer stimuli generally had more influence than bacteria↔buffer
434 stimuli in states 1 and 2, and less influence in state 3 (Fig. 4B). While the state-agnostic decoding
435 model found no difference between channel 1 and channel 2 buffer flows in how they drove AVA
436 and RME cluster activity (Fig. 2K-L), the SDT-MLR model found that the channel 1 buffer had a
437 greater effect on AVA and RME cluster activity than the channel 2 buffer in states 2, 3, and 4 (Fig.
438 4B, gray). This bias may be due to channel 1 being closer to the *C. elegans* nose, as previously
439 surmised. However, this bias disappeared when bacteria was included in the sensory context
440 (Fig. 4B, cyan). Therefore, while channel 2 is chemically the same for both buffer↔buffer and

441 bacteria↔buffer stimulus sequences, the effect that the channel 2 buffer had on AVA and RME
442 cluster activity changed depending on whether the greater sensory context involves switching
443 between chemically identical buffers, or switching between bacterial stimuli and buffer.

444
445

446 Discussion

447

448 Here, we demonstrate that the SDT–MLR model can identify interpretable global network states
449 that underlie differential gating of sensory input at the motor and command neuron level. First, we
450 used state-agnostic encoding and decoding models to confirm that bacteria onset and removal
451 differ in how they drive activity of sensory neurons, AVA, and RME clusters. Using the SDT–MLR
452 model, we identified two sensory-unresponsive network states (states 1 and 2) and two sensory-
453 responsive network states (states 3 and 4) in the bacteria↔buffer sensory context. For each
454 network state, we explicitly characterized how the history of each of the four functionally defined
455 motor/command neural populations (AVA, RME, SMDD, SMDV) drive AVA and RME cluster
456 activity to produce each network state. Finally, we used the SDT–MLR model to identify how
457 sensory input in general, as well as stimulus features and sensory context in particular, influence
458 AVA and RME cluster activity.

459 The encoding model showed that sensory neural responses to the addition of bacterial
460 stimuli (ON) and its removal (OFF) can be modeled by two linear ordinary differential equations
461 using one fast and one slow filter. Linearity in sensory neurons is observed in both vertebrates
462 and invertebrate photoreceptors (43), rat trigeminal neurons (44), and primate vestibular neurons
463 (45), implying that this might be a common phenomenon. We also show that ON sensory neurons
464 perfectly adapt to the bacterial stimulus, consistent with previous studies (38), while OFF neurons
465 adapt imperfectly. Given that our analysis included all sensory neurons responding to bacterial
466 stimuli, we suggest that this might be a general principle of *C. elegans* sensory neurons. Similar
467 differences in adaptation in ON and OFF neurons are also observed in single-cell
468 electrophysiological recordings from vertebrate photoreceptors and olfactory sensory neurons
469 (46). Moreover, these results also provide some hints about the encoding strategies of these two
470 sensory-neuron classes. We suggest that ON neurons encode stimulus over a larger dynamic
471 range compared to OFF neurons. Consistently, we have previously shown that AWA sensory
472 neurons (ON) have a larger dynamic range compared to AWC sensory neurons (OFF) in
473 detecting benzaldehyde (47). Moreover, studies in the vertebrate retina have shown that the
474 dynamic range of the ON pathway is much greater than that of the OFF pathway, likely due to a
475 selective effect of pre-synaptic inhibition on the ON, but not OFF, bipolar cells (48), confirming the
476 validity of our hypothesis.

477 The decoding model informed which motor/command neural populations were targets of
478 the sensory input, and also served as a state-agnostic model to compare with the state-
479 dependent SDT–MLR model. Both models were used to assess how sensory input affects AVA
480 and RME cluster activity. While the decoding model found no difference in effect between either
481 of the buffer channels in buffer↔buffer stimulus sequences, the SDT–MLR model revealed that
482 buffer↔buffer sensory input does indeed have a channel bias that is more pronounced in some
483 states than others. This suggests that the SDT–MLR model is more sensitive to sensory effect
484 compared to the decoding model. This sensitivity is further amplified by subdividing sensory
485 effects by state, channel, sensory neuron classification (ON/OFF), prediction class (AVA rise,
486 AVA fall, RME rise, RME fall), and stimulus features (high-variance pulses, low-variance pulses).
487 This granular approach allowed us to identify specific sensory effects that were obscured in more
488 general analyses. We found that high-variance and low-variance pulses had similar influences in
489 one state, but sensory input from low-variance pulses were gated more heavily in another state.
490 Additionally, we revealed that state-dependent gating of buffer stimulus is dependent on whether
491 the greater sensory context involves switching between bacteria and buffer, or between buffer
492 and buffer.

493 The SDT–MLR model differs in both goal and interpretability from recent studies that
494 described network states in *C. elegans* whole-brain activity (25, 27, 37, 49). In these studies,

495 whole-brain activity is analyzed with the purpose of understanding the temporal dynamics of
496 neuronal populations in terms of how the network state evolves over time. Often, probabilities of
497 network state transitions are related to corresponding stimulus or behavioral transitions. A
498 dimensionality reduction technique called principal component analysis (PCA) (50) is used to
499 quantify brain-wide correlations that reflect signals shared by clusters of neurons. These shared
500 signals are referred to as temporal principal components (PCs). A key operation of PCA-based
501 analyses is to transform whole-brain activity to new axes defined by the top PCs that explain the
502 most variance in data. However, the meaningful linear axes that originally described the data are
503 lost in the process. While PCA-based analyses are useful for distinguishing between network
504 states and their transition between each other, these networks states and transitions are
505 described in terms of PCs, which can be difficult to interpret. Nonetheless, PC weights can still be
506 used to identify relevant neurons and activity trends associated with each state (25, 27, 37, 49).
507 In our study, we are less concerned with the probabilities of transitioning between states, and
508 more interested in the within-state conditional probabilities of individual neuronal populations
509 interacting with each other. Instead of using PCA, our model preserves interpretability by using
510 soft decision trees, such that network states and network interactions are always described by the
511 identities of neuronal populations and their corresponding activity patterns. Rather than
512 supplanting PCA-based analyses, our SDT–MLR model serves as a complementary method for
513 focusing on the network interactions within individual network states rather than the temporal
514 dynamics that connect those network states.

515 Interestingly, the sensory-responsive states identified by the SDT–MLR are characterized
516 by neural activity that has been previously shown to be associated with forward locomotion, while
517 the sensory-unresponsive states are characterized by neural activity associated with reverse
518 locomotion. This is consistent with previous reports showing that inhibition of sensory input
519 occurs at particular phases of the locomotory cycle (11, 12). Inhibition of sensory input during
520 movement may serve to distinguish between external stimuli and self-generated stimuli (51),
521 which is accomplished by integrating sensory inputs with motor inputs (corollary discharge) (52).
522 Since typical *C. elegans* locomotion consists primarily of forward locomotion punctuated by
523 transient reversals (53), one possibility is that sensation of stimuli is suppressed during reversals
524 to temporarily pause processing of stimulus flows until a stable locomotion state is restored. It is
525 important to note that our study was conducted with *C. elegans* trapped in an immobilized
526 position in a microfluidic chip, and therefore behavioral associations were inferred purely from
527 motor and command neuron activity. Moreover, a recent study showed that the set of neurons
528 correlated with AVA differs depending on whether *C. elegans* is immobilized or freely moving
529 (49). Thus, our association of AVA and RME clusters activity with forward and reverse locomotion
530 is tentative and should be confirmed in freely moving animals. However, while imaging freely
531 moving *C. elegans* would provide rich behavioral information that can be added to the SDT–MLR
532 model, complex and precise stimuli presentation can be difficult to achieve when the stimulus
533 target is mobile. There are some efforts to study sensation in freely moving animals (22, 54), and
534 a reasonable balance of behavioral and sensory information richness may be achieved with a
535 microfluidic chip that allows semi-restricted locomotion and somewhat fast waves of liquid stimuli
536 (55).

537 Overall, we present an approach for understanding how sensory information filters
538 through whole-brain network interactions to affect downstream motor and command neurons in a
539 state-dependent manner. Currently, there is an epistemological bias towards identifying network
540 states that correspond with a particular stimulus or motor state. In contrast, there has been less
541 focus on network states that are defined by altered network interactions. Our computational
542 approaches provide a method for investigating network mechanisms at the level of pairwise
543 interactions between neuronal populations. While our study only looked at the network
544 mechanisms underlying sensorimotor integration, this model can be leveraged to also understand
545 how network inputs are integrated at any network level. More broadly, we suggest that our
546 approach of combining soft decision trees with multinomial logistic regression can be used to
547 identify relationships, not only in neural networks, but also in cellular signaling pathways,
548 transcription factor networks, and between other complex biological or physical entities.

549

550 **Materials and Methods**

551

552 **Whole-brain imaging**

553 We used two transgenic strains that expressed GCaMP. The primary strain (ZIM294) expressed
554 GCaMP5K in the nuclei of all neurons (*mzmEx199 [Punc-31::NLSGCaMP5K; Punc-122::GFP]*).
555 To identify neurons associated with activity patterns observed in ZIM294, we used a strain
556 (OH15500) that expressed GCaMP6s and NeuroPAL (*otIs669[NeuroPAL];otIs672[Panneuronal*
557 *GCaMP6s]*). Cells were identified according to the map described by Yemini and colleagues (24).
558 We monitored changes in GCaMP fluorescence using a Zeiss LSM 880 with Airyscan. Acquisition
559 was done in 2 micron z-steps. In 'Fast' mode, the Airyscan images the entire head of the adult
560 worm at about 1.5 volumes per second. Worms were typically imaged for approximately ten
561 minutes. We then used piecewise rigid registration to remove motion artefacts (56) and non-
562 negative matrix factorization to isolate individual neurons and extract their fluorescence values
563 (33). Out of a total 189 neurons in the head, our approach identified 50-100 neurons per animal.
564

565 **Stimulus delivery**

566 Day 1 adult animals were washed in M9 and loading into in a microfluidic device that trapped the
567 worm body while exposing only the nose to stimulus flows (28). Animals were also treated with
568 1.5 mMol of the paralytic tetramisole hydrochloride to suppress most perceivable worm
569 movement. The movement of untreated worms proved too difficult to motion correct. We
570 delivered precise patterns of fluctuating bacteria and M9 buffer liquid flows using a custom
571 designed Arduino device to send pulses to a valve controller. The bacteria solution was prepared
572 as a 1:1 resuspension of a bacterial culture ($OD_{600} = 0.4$) in M9 buffer as previously described
573 (29). The controller determines whether bacteria or buffer is routed to the nose of the trapped
574 worm or away from the worm. Worms were exposed to binary patterns of bacteria and buffer. A
575 number of different stimulus protocols are used in this study. In the base protocol, the trial is
576 divided up into pulse blocks of ~15 seconds. The pattern is constructed using transition
577 probabilities: $p(\text{switch on} | \text{off}) = 0.2$ and $p(\text{switch off} | \text{on}) = 0.4$. In the faster protocols, the same
578 switch probabilities are used but the pulse blocks have length ~1.5 seconds. The patterned
579 protocols are effectively the same as the base protocol. The only difference is that their 'stimulus
580 on blocks' are composed of multiple pulses.
581

582 **GCaMP filters**

583 The GCaMP filter $g(x)$ is modeled as a difference of exponentials with parameters matching those
584 of Chen and colleagues (32). This procedure is complicated by the volumetric nature of the
585 imaging data. Consider two sensory neurons with identical calcium dynamics; they respond to
586 stimulus with the same timescale. Neuron A is in imaging slice 0, while neuron B is in slice 7.
587 These two neurons will have the same calcium timings relative to the stimulus. However, Neuron
588 B will appear to have faster response kinetics since it is acquired over half a second later (relative
589 to stimulus onset/removal) compared to neuron A. Thus, the slice in which the neuron appears
590 needs to be considered in the creation of its GCaMP filter:

$$g_f(t) = \int_{t_1}^{t_2} g(x) dx$$
$$t_1 = t + \frac{z}{n_z}$$
$$t_2 = t + \frac{z+1}{n_z}$$

592 where $g(x)$ refers to the difference of exponentials and n_z refers to the number of z slices. The
593 normalized $g(t)$ filter is applied via a linear convolution to transition between calcium and GCaMP
594 dynamics.
595

596 **ON and OFF sensory neuron classification**

597 Sensory neurons were classified as either ON or OFF for neuronal activity collected during
598 bacteria↔buffer stimulus sequences. The change in normalized fluorescence over a series of ≥
599 10 stimulus pulses (all trials have at least a few of these). Both the first 10 volumes into a bacteria
600 pulse and the first 10 volumes into a buffer pulse (following bacterial removal) were considered.
601 The following metric was then calculated:

$$rank = \left(\sum_i^P (f(t_i + 10) - f(t_i)) \right) - \left(\sum_j^Q (f(t_j + 10) - f(t_j)) \right)$$

603 where f is normalized fluorescence, t is pulse onset, P is the number of bacteria pulses, and Q is
604 the number of buffer pulses. The cells with the highest ranks considered as potential ON cells,
605 and the cells with the lowest ranks were considered as potential OFF cells. Rank cutoffs were
606 selected manually for each trial. ON cells were categorized as those neurons that obviously and
607 immediately increased activity upon bacteria onsets, and immediately decreased upon bacteria
608 removals (Fig. 11). In contrast, OFF cells were classified as neurons that decreased activity upon
609 bacteria onsets and increased upon bacteria removals. For both ON and OFF cells, baseline (low
610 variance) activity occurred when the stimulus of interest was absent (during buffer pulses). This
611 distinguishes OFF-bacteria sensory neurons from hypothetical ON-buffer sensory neurons, for
612 which baseline activity would occur during bacteria pulses.

613

614 **Encoding model**

615 The encoding model predicted ON and OFF sensory neuron activity from stimulus features. The
616 core primary sensory model consists of three parts: (1) a set of cascade basis functions, (2)
617 coefficients for the basis functions, and (3) a GCaMP transformation.

618

$$\begin{aligned} \frac{dx_i}{dt} &= \tau \cdot ([input] - x_i(t)) \\ X(t) &= \sum a_i x_i(t) \\ g(t) &= (x^p \otimes f_g)(t) \end{aligned}$$

620

621 where $x(t)$ is the inferred calcium level of the cell and is calculated as the sum of the temporal
622 filters (ODE model solutions), f_g is the GCaMP filter, and p is a positive value required for the
623 GCaMP transformation. The fitting procedure learns values for the time constant τ and the basis
624 coefficients a_i . This model uses the solutions to these ordinary differential equations $x_i(t)$ as
625 basis functions. For a given model instantiation, each equation is assigned a value for τ . After the
626 ordinary differential equations are solved analytically, the model can be linearized, allowing for
627 robust estimates of the a_i coefficients (see Methods). We then used a random search strategy to
628 obtain estimates of τ . Moreover, by toggling the coefficient constraint, we can test whether perfect
629 adaptation is necessary to predict sensory neuron activity. This constraint yields perfect
630 adaptation as all the ordinary differential equation basis functions saturate at the same value
631 ($[input]$).

632

633 We used a random search strategy to find the correct set of basis functions. The strategy
634 chooses N basis time constants for an N cascade model and an initial estimate of p power. It
635 solves the basis equations analytically for a given stimulus pattern and produces an initial
636 estimate for the coefficients by fitting to a linearized approximation of the neuron's calcium trace.
637 In this approximation, the raw sensory neuron fluorescence trace is deconvolved using the
638 Richardson-Lucy method (57) and taken to the $(1/p)$ power. The initial estimate for the
639 coefficients is the solution to the resulting linear regression equation. Finally, this system fits the
640 full model (free variables consist of basis coefficients and p power) is fit to the raw fluorescence
641 trace using gradient descent. We then repeat this process for a large number of random searches
642 to define the basis functions.

643 **Decoding model**

644 The decoding model predicted stimulus states activity from stimulus features. For both the
645 decoding and prediction analyses, we split the data into contiguous blocks of ~10 second (16
646 volume) duration. Within each block, subwindows were created in a rolling fashion. For instance,
647 for an N volume prediction window, there are $16-N$ legal, overlapping subwindows within each
648 block. It should be noted that there is no overlap between prediction windows of adjacent blocks.
649 Test/train sampling is done at the block level, guaranteeing no train/test prediction overlap. This
650 system captures sharp transitions while measuring targets over multiple time bins, thereby
651 limiting noise in the targets. We chose a length of 16 volumes because this captures the entirety
652 of motor neuron event initiation (for all motor neuron classes). This causes bootstrap sampling to
653 be performed at the event level, stopping a small, handful of events from dominating model
654 outcomes. We did not test other bootstrap sizes.

655 We used Gaussian basis functions for both decoding and prediction tasks. This involves
656 filtering network history and stimulus data through these basis functions before being fed into
657 decoding and prediction models. We chose specific gaussians (parametrized by mean and
658 variance) by hand-tuning model performance on the hyperparameter set.

659 Given the choice of 16 volume blocks and 8 volume time windows, there are $16-8=8$
660 prediction windows within each time block. Unlike the prediction task, the decoding task centers
661 the prediction windows relative to the input data. For instance, in one decoding task, RME/AVA
662 cell cluster data from $t+4-8$ to $t+4+8$ volumes is used to predict whether the stimulus is
663 on/off/alterd from t to $t+8$ volumes. The unit of 8 volumes was chosen because many of the
664 pulse protocols use 10 volume pulses as a base unit. Thus, using 8 volumes guarantees a fair
665 number of samples of the on stimulus class. We did not test other volume lengths.

666 In the decoding analyses, we predict five classes of stimulus patterns from network
667 activity (58). Prediction from worm identity alone serves as the null model for all decoding
668 analyses. In order to ensure best performance for the null model, we balanced the classes within
669 each worm. For each worm, if there are N occurrences of class A in the training set, there are N
670 occurrences of class A in the test set. We ensured this by randomly removing prediction windows.

671

672 **SDT-MLR model**

673 We used different L1 norms for each of the multinomial logistic regression input classes:
674 AVA/RME/SMDV/SMDD terms, ON/OFF cell terms, and worm identity terms. The worm identity
675 terms essentially make the forecasting models into a random-intercept model (59). Initial
676 experiments found no benefit in random-intercept style models. The number of network states
677 and number/shape of gaussian filters were additional hyperparameters. A combination of hand-
678 turning and grid search were used on the hyperparameter set to find good regularizers. This
679 hyperparameter set was also used for the soft decision tree, which could also be thought of as an
680 additional hyperparameter in this study. These hyperparameters were frozen on the out-of-
681 bootstrap analysis (42).

682 In the forecasting task, we predicted changes in GCaMP fluorescence from time t to $t+T1$
683 using network history from $t-T2$ to t and sensory neuron activity from $t-T2+T1$ to $t+T1$. We used a
684 length of twenty-four volumes for $T2$ for all prediction analyses. We treated the length of $T1$ as an
685 additional hyperparameter. As in the decoding analysis, these prediction windows are contained
686 inside larger data blocks. We performed train/test sampling at the block level. We chose sixteen
687 seconds (24 volumes) for $T1$ in all models, as 16 seconds is sufficient to capture the majority of
688 command neuron events.

689 RME and AVA activation and inactivation is clearly probabilistic. We used a multinomial
690 logistic regression (MLR) as the base model for motor-neuron activity prediction. In order to use
691 MLR, we discretized GCaMP fluorescence activity in every prediction window. This is done by
692 subtracting the average GCaMP fluorescence over the prediction window by the GCaMP
693 fluorescence level at the beginning of that window.

694 RME and AVA neurons have non-linear calcium dynamics. Two of these features are
695 boundedness and momentum. Members of the AVA cluster exhibit boundedness: their activity is
696 limited to a range between their upper and lower stable states. Also, activity in these neurons

697 appears to have momentum: when one of these neurons begins a transition between the stable
698 states, it will tend to complete that transition. A single, linear model is unable to describe both
699 momentum and boundedness. It must learn the positive correlation between a future AVA rise
700 and past AVA activity to capture momentum. However, this positive correlation should weaken
701 and become negative as AVA nears its upper bound, since AVA activity does not rise above this
702 bounded limit. Thus, a gating model is required to capture the change in this positive correlation.

703 Here, we employ multinomial logistic regression (MLR) models to capture nonlinear
704 dynamics, allowing us to capture features like momentum and boundedness. A gating model is
705 used to divide the space of network histories into subspaces. Each of these different subspaces
706 is associated with a different MLR model. This approach with two submodels can simultaneously
707 model both momentum and boundedness in AVA. In one theoretical solution, one MLR submodel
708 is only active when the AVA cell cluster is near its lower bound, while another is active when AVA
709 near its upper bound. The first submodel learns a positive correlation between a past AVA
710 increase in activity and future AVA rise (momentum), while the second learns a weak positive or
711 negative correlation (boundedness).

712 We use a hybrid model combining soft decision trees and multinomial logistic regression
713 (SDT-MLR) method to divide the network trajectory space into different subspaces. We assumed
714 that GCaMP fluorescence changes in each of these subspaces can be well-described by an
715 MLR. A soft decision tree is a form of oblique decision tree that is end-to-end differentiable (40).
716 Each branch of the soft decision tree is a different logistic regression model on the same input
717 vector, which outputs a left vs right probability. These left and right probabilities are multiplied by
718 the predicted class probabilities of the corresponding left and right subtrees. In this manner, soft
719 decision trees are essentially hierarchical filters that can be learned through gradient descent.
720 The outputs of the soft decision tree weigh the different MLR models. For instance, a soft
721 decision tree with depth 2 and width 2 will have 4 output states. Each of these output states are
722 associated with a different MLR. All of these MLRs are trained against the entire dataset.
723 However, the data points are weighted by the particular soft decision tree output leaf. Hence,
724 different MLR models will focus on different subsets of the data.

725 We found that averaging predictions across SDT-MLR models improves cross-validation
726 performance. This averaging is done at two levels. First, within a SDT-MLR model, the
727 predictions of each MLR are weighted by the soft decision tree and averaged. Second, these
728 averaged predictions are further averaged across several SDT-MLR models. Here, twenty-five
729 SDT-MLR models were fit separately to the hyperparameter set. The best hybrid model was
730 chosen for analysis on the cross-validation set. For training on the cross-validation set, the Soft
731 Trees were frozen; only the MLRs were trained. Hence, training is convex (weighted multinomial
732 logistic regression) on the cross-validation set. Freezing the soft decision during cross-validation
733 allows us to easily align model data across bootstraps. This, in turn, gives us information on the
734 variance of different features of the MLR models.

735 In our exploration of the hyperparameter set, we found that SDT-MLR models tend to
736 converge on bad solutions if not regularized. These bad solutions are characterized by poor
737 training and test set performance as well as state imbalance. The Soft Tree assigns most data
738 points to one of its submodels, while its other MLR submodels are trained on very small subsets
739 of the data resulting in state imbalance. We solved this issue by maximizing entropy regularizer
740 $H(X)$:

$$V_k(X) = \frac{1}{N} \sum_i^N S_k(X_i)$$
$$H(X) = \sum_k V_k(X) \log \left(\frac{1}{V_k(X)} \right)$$

742 where X_i is the i^{th} input data point in the minibatch. S_k is the probability assigned to the k th
743 state/submodel by the soft decision tree. Thus, V_k is the average probability of state k across the
744 minibatch. Therefore, $H(X)$ is high when all states are equally represented in the minibatch. It
745 should be noted that this regularizer does not directly penalize high state probabilities.

746 **Division of stimulus sequences**

747 To compare the effect of short versus long stimulus pulses in the SDT–MLR model, complete
748 stimulus sequences were divided into low-variance (long pulses) and high-variance (short pulses)
749 stimulus patterns. Low-variance stimulus patterns were constructed by dividing the trial into pulse
750 blocks of ~15 seconds, with the transition probabilities $p(\text{switch on} | \text{off}) = 0.2$ and $p(\text{switch off} |$
751 $\text{on}) = 0.4$. High-variance stimulus patterns were also constructed by dividing the trial into bacteria
752 or buffer blocks with the same transition probabilities as for low-variance stimulus patterns. The
753 difference between low- and high- variance stimulus patterns is that the bacteria block consists of
754 a series of sub-pulses rather than a single constant pulse. These sub-pulses are ~3 seconds
755 bacteria and ~3 seconds buffer.

756 **Acknowledgments**

757 We thank Manuel Zimmer, Oliver Hobert and CGC (Caenorhabditis Genetics Center) for worm
758 strains and Uri Manor, Tong Zhang and the Waitt Advanced Biophotonics Center for advice and
759 assistance with our imaging experiments. We also thank Saket Navlakha, Ryan Rowekamp,
760 Javier How, Molly Matty, Jessica Haley, Michael Rieger, and Eric Edsinger for discussions and
761 comments on the manuscript. This work was supported by grants from the National Institutes of
762 Health NIH 5R01MH096881 (S.H.C.); 5T32DK007328-35, 5T32DK007328-37, 5T32MH015174-
763 37 and 5T32MH015174-38 (E.Y.). U19NS112959, P30AG068635, AHA-Allen Initiative in Brain
764 Health and Cognitive Impairment award 19PABH134610000 (T.O.S.). Z.T.C. was supported by a
765 fellowship from the Dan and Marina Lewis Foundation. K.T.Q. is supported by a Postdoctoral
766 fellowship from the Paul F. Glenn Foundation. CGC is funded by the NIH Office of Research
767 Infrastructure Programs (P40 OD010440).

770 **References**

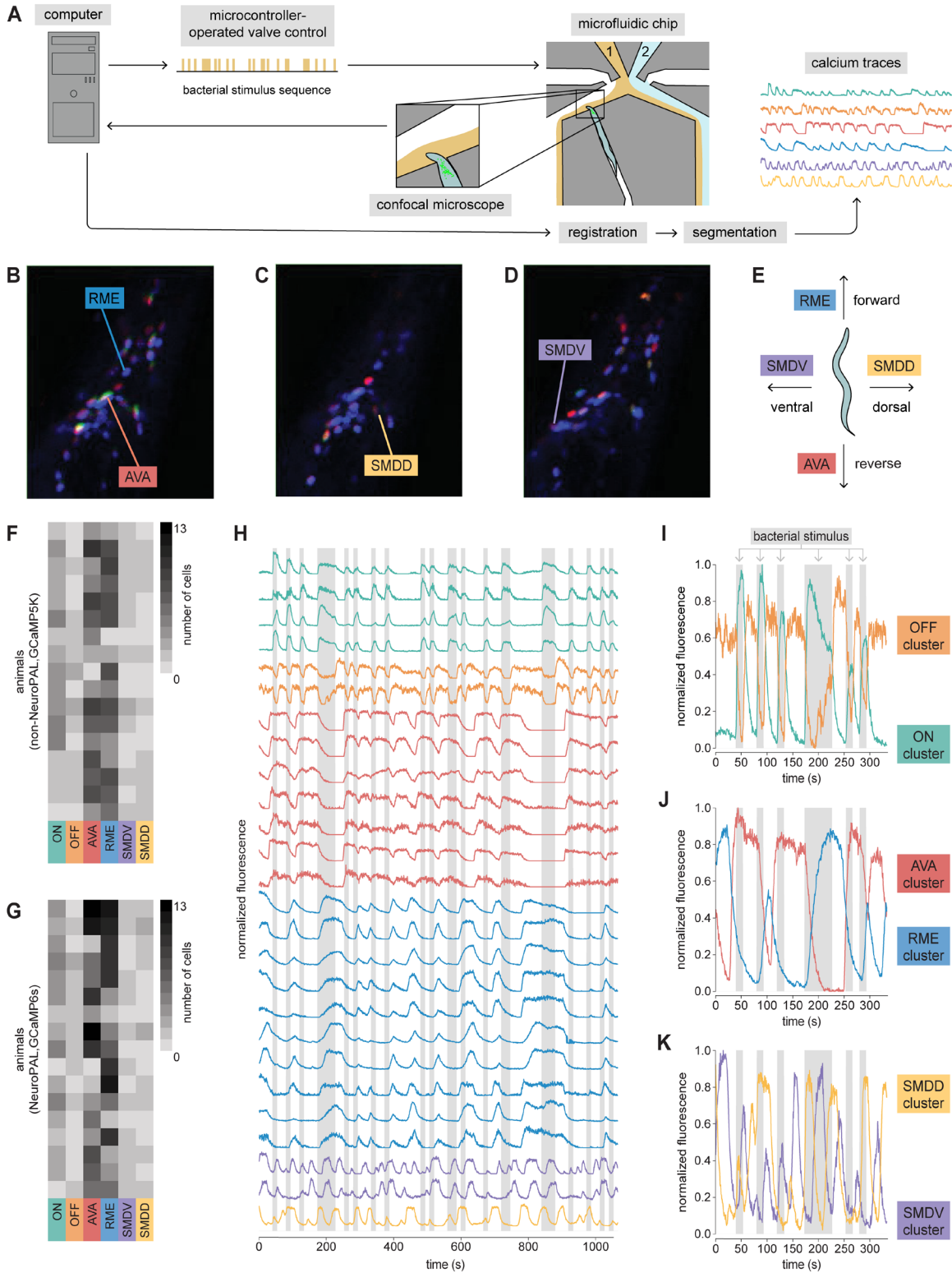
- 771 1. J. M. Beck, W. J. Ma, X. Pitkow, P. E. Latham, A. Pouget, Not noisy, just wrong: the role
772 of suboptimal inference in behavioral variability. *Neuron* **74**, 30-39 (2012).
- 773 2. L. C. Osborne, S. G. Lisberger, W. Bialek, A sensory source for moto variation. *Nature*
774 **437**, 412-416 (2005).
- 775 3. J. H. Reynolds, D. J. Heeger, The normalization model of attention. *Neuron* **61**, 168-185
776 (2009).
- 777 4. J. H. Reynolds, T. Pasternak, R. Desimone, Attention increases sensitivity of V4 neurons.
778 *Neuron* **26**, 703-714 (2000).
- 779 5. P. Sörqvist, S. Stenfelt, J. Rönnerberg, Working memory capacity and visual–verbal
780 cognitive load modulate auditory–sensory gating in the brainstem: Toward a unified view
781 of attention. *J. Cogn. Neurosci.* **24**, 2147-2154 (2012).
- 782 6. A. Schoups, R. Vogels, N. Qian, G. Orban, Practising orientation identification improves
783 orientation coding in V1 neurons. *Nature* **412**, 549-553 (2001).
- 784 7. A. F. Teich, N. Qian, Learning and adaptation in a recurrent model of V1 orientation
785 selectivity. *J. Neurophysiol.* **89**, 2086-2100 (2003).
- 786 8. A. A. Faisal, L. P. Selen, D. M. Wolpert, Noise in the nervous system. *Nat. Rev. Neurosci.*
787 **9**, 292-303 (2008).
- 788 9. M. N. Shadlen, K. H. Britten, W. T. Newsome, J. A. Movshon, A computational analysis of
789 the relationship between neuronal and behavioral responses to visual motion. *J*
790 *Neurosci.* **16**, 1486-1510 (1996).
- 791 10. Z. W. Davis, L. Muller, J. Martinez-Trujillo, T. Sejnowski, J. H. Reynolds, Spontaneous
792 travelling cortical waves gate perception in behaving primates. *Nature* **587**, 432-436
793 (2020).
- 794 11. K. T. Sillar, A. Roberts, A neuronal mechanism for sensory gating during locomotion in a
795 vertebrate. *Nature* **331**, 262-265 (1988).

- 798 12. M. H. Ouellette, M. J. Desrochers, I. Gheta, R. Ramos, M. Hendricks, A Gate-and-Switch
799 Model for Head Orientation Behaviors in *Caenorhabditis elegans*. *eNeuro* **5** (2018).
800 13. E. Eggermann, Y. Kremer, S. Crochet, C. C. Petersen, Cholinergic signals in mouse
801 barrel cortex during active whisker sensing. *Cell reports* **9**, 1654-1660 (2014).
802 14. J. M. Blackwell, M. N. Geffen, Progress and challenges for understanding the function of
803 cortical microcircuits in auditory processing. *Nat. Commun.* **8**, 1-9 (2017).
804 15. M. M. Churchland, J. P. Cunningham, M. T. Kaufman, J. D. Foster, P. Nuyujukian, *et al.*,
805 Neural population dynamics during reaching. *Nature*, **487**, 51-56 (2012).
806 16. R. C. Williamson, B. Doiron, M. A. Smith, M. Y. Byron, Bridging large-scale neuronal
807 recordings and large-scale network models using dimensionality reduction. *Curr. Opin.*
808 *Neurobiol.* **55**, 40-47 (2019).
809 17. M. B. Ahrens, J. M. Li, M. B. Orger, D. N. Robson, A. F. Schier, *et al.*, Brain-wide
810 neuronal dynamics during motor adaptation in zebrafish. *Nature* **485**, 471-477 (2012).
811 18. M. B. Ahrens, M. B. Orger, D. N. Robson, J. M. Li, P. J. Keller, Whole-brain functional
812 imaging at cellular resolution using light-sheet microscopy. *Nat Methods* **10**, 413-420
813 (2013).
814 19. W. C. Lemon, S. R. Pulver, B. Höckendorf, K. McDole, K. Branson, *et al.*, Whole-central
815 nervous system functional imaging in larval *Drosophila*. *Nat. Commun.* **6**, 1-16 (2015).
816 20. T. Schrödel, R. Prevedel, K. Aumayr, M. Zimmer, A. Vaziri, Brain-wide 3D imaging of
817 neuronal activity in *Caenorhabditis elegans* with sculpted light. *Nat. Methods* **10**, 1013-
818 1020 (2013).
819 21. J. P. Nguyen, F. B. Shipley, A. N. Linder, G. S. Plummer, M. Liu, *et al.* (2016). Whole-
820 brain calcium imaging with cellular resolution in freely behaving *Caenorhabditis*
821 *elegans*. *Proceedings of the National Academy of Sciences*, **113**(8), E1074-E1081.
822 22. V. Venkatachalam, N. Ji, X. Wang, C. Clark, J. K. Mitchell, *et al.*, Pan-neuronal imaging in
823 roaming *Caenorhabditis elegans*. *Proc. Natl. Acad. Sci. U. S. A.* **113**, E1082-E1088
824 (2016).
825 23. J. J. How, S. Navlakha, S. H. Chalasani, Neural network features distinguish
826 chemosensory stimuli in *Caenorhabditis elegans*. *bioRxiv* [Preprint] (2020).
827 <https://www.biorxiv.org/content/10.1101/2020.02.18.955245v1> (accessed 31 October
828 2021).
829 24. E. Yemini, A. Lin, A. Nejatbakhsh, E. Varol, R. Sun, *et al.*, NeuroPAL: a multicolor atlas
830 for Whole-Brain neuronal identification in *C. elegans*. *Cell* **184**, 272-288 (2021).
831 25. S. Kato, H. S. Kaplan, T. Schrödel, S. Skora, T. H. Lindsay, *et al.*, Global brain dynamics
832 embed the motor command sequence of *Caenorhabditis elegans*. *Cell*, **163**, 656-669
833 (2015).
834 26. A. L. Nichols, T. Eichler, R. Latham, M. Zimmer, A global brain state underlies *C. elegans*
835 sleep behavior. *Science* **356** (2017).
836 27. S. Skora, F. Mende, M. Zimmer, Energy scarcity promotes a brain-wide sleep state
837 modulated by insulin signaling in *C. elegans*. *Cell Rep.* **22**, 953-966 (2018).
838 28. N. Chronis, M. Zimmer, C. I. Bargmann, Microfluidics for in vivo imaging of neuronal and
839 behavioral activity in *Caenorhabditis elegans*. *Nat. Methods* **4**, 727-731 (2007).
840 29. A. J. Calhoun, A. Tong, N. Pokala, J. A. Fitzpatrick, T. O. Sharpee, *et al.* Neural
841 mechanisms for evaluating environmental variability in *Caenorhabditis elegans*. *Neuron*
842 **86**, 428-441 (2015).
843 30. S. H. Chalasani, N. Chronis, M. Tsunozaki, J. M. Gray, D. Ramot, *et al.*, Dissecting a
844 circuit for olfactory behaviour in *Caenorhabditis elegans*. *Nature* **450**, 63-70 (2007).
845 31. J. Akerboom, N. Carreras Calderón, L. Tian, S. Wabnig, M. Prigge, *et al.* Genetically
846 encoded calcium indicators for multi-color neural activity imaging and combination with
847 optogenetics. *Front Mol Neurosci.* **6** (2013).
848 32. T. W. Chen, T. J. Wardill, Y. Sun, S. R. Pulver, S. L. Renninger, *et al.*, Ultrasensitive
849 fluorescent proteins for imaging neuronal activity. *Nature* **499**, 295-300 (2013).
850 33. E. A. Pnevmatikakis, D. Soudry, Y. Gao, T. A. Machado, J. Merel, *et al.* Simultaneous
851 denoising, deconvolution, and demixing of calcium imaging data. *Neuron*, **89**(2), 285-299.

- 852 34. Hendricks, M., Ha, H., Maffey, N., Zhang, Y. (2012). Compartmentalized calcium
853 dynamics in a *C. elegans* interneuron encode head movement. *Nature* **487**, 99-103
854 (2016).
- 855 35. Y. Shen, Q. Wen, H. Liu, C. Zhong, Y. Qin, *et al.*, An extrasynaptic GABAergic signal
856 modulates a pattern of forward movement in *Caenorhabditis elegans*. *Elife* **5**, e14197
857 (2016)..
- 858 36. A. Kocabas, C. H. Shen, Z. V. Guo, S. Ramanathan, Controlling interneuron activity in
859 *Caenorhabditis elegans* to evoke chemotactic behaviour. *Nature* **490**, 273-277 (2012).
- 860 37. H. S. Kaplan, O. S. Thula, N. Khoss, M. Zimmer, Nested neuronal dynamics orchestrate
861 a behavioral hierarchy across timescales. *Neuron* **105**, 562-576 (2020).
- 862 38. S. Kato, Y. Xu, C. E. Cho, L. F. Abbott, C. I. Bargmann, Temporal responses of *C.*
863 *elegans* chemosensory neurons are preserved in behavioral dynamics. *Neuron* **81**, 616-
864 628 (2014).
- 865 39. D. W. Hosmer, S. Lemeshow, R. X. Sturdivant. *Applied logistic regression* (Wiley, 2000)
- 866 40. N. Frosst, G. Hinton, Distilling a neural network into a soft decision tree. *arXiv* [Preprint]
867 (2017). <https://arxiv.org/abs/1711.09784> (accessed 31 October 2021).
- 868 41. S. Linderman, A. Nichols, D. Blei, M. Zimmer, L. Paninski, Hierarchical recurrent state
869 space models reveal discrete and continuous dynamics of neural activity in *C.*
870 *elegans*. *BioRxiv* [Preprint] (2019). <https://www.biorxiv.org/content/10.1101/621540v1>
871 (accessed 31 October 2021).
- 872 42. I. Tsamardinos, E. Greasidou, G. Borboudakis, Bootstrapping the out-of-sample
873 predictions for efficient and accurate cross-validation. *Machine Learning* **107**, 1895-1922
874 (2018).
- 875 43. J. Pahlberg, A. P. Sampath, Visual threshold is set by linear and nonlinear mechanisms
876 in the retina that mitigate noise: How neural circuits in the retina improve the signal-to-
877 noise ratio of the single-photon response. *Bioessays* **33**, 438-447 (2011).
- 878 44. L. M. Jones, D. A. Depireux, D. J. Simons, A. Keller, Robust temporal coding in the
879 trigeminal system. *Science* **304**, 1986-1989 (2004).
- 880 45. C. Massot, A. D. Schneider, M. J. Chacron, K. E. Cullen, The vestibular system
881 implements a linear–nonlinear transformation in order to encode self-motion. *PLoS*
882 *Biol.* **10**, e1001365 (2012).
- 883 46. G. De Palo, G. Facchetti, M. Mazzolini, A. Menini, V. Torre, C. Altafini, Common
884 dynamical features of sensory adaptation in photoreceptors and olfactory sensory
885 neurons. *Sci. Rep.*, **3**, 1-8 (2013).
- 886 47. S. G. Leinwand, C. J. Yang, D. Bazopoulou, N. Chronis, J. Srinivasan, *et al.*, Circuit
887 mechanisms encoding odors and driving aging-associated behavioral declines in
888 *Caenorhabditis elegans*. *Elife* **4**, e10181 (2015).
- 889 48. B. T. Sagdullaev, M. A. McCall, P. D. Lukasiewicz, Presynaptic inhibition modulates
890 spillover, creating distinct dynamic response ranges of sensory output. *Neuron* **50**, 923-
891 935 (2006).
- 892 49. K. M. Hallinen, R. Dempsey, M. Scholz, X. Yu, A. Linder, *et al.*, Decoding locomotion
893 from population neural activity in moving *C. elegans*. *Elife* **10**, e66135 (2021).
- 894 50. I.T. Jolliffe, Principal Component Analysis, Second Edition (Springer, 2002).
- 895 51. H. Straka, J. Simmers, B. P. Chagnaud, A new perspective on predictive motor
896 signaling. *Curr. Biol.* **28**, R232-R243 (2018).
- 897 52. T. B. Crago, M. A. Sommer, Corollary discharge across the animal kingdom. *Nat. Rev.*
898 *Neurosci.* **9**, 587-600 (2008).
- 899 53. N. A. Croll, Components and patterns in the behaviour of the nematode *Caenorhabditis*
900 *elegans*. *J. Zoology* **176**, 159-176 (1975).
- 901 54. V. Susoy, W. Hung, D. Witvliet, J. E. Whitener, M. Wu, *et al.*, Natural sensory context
902 drives diverse brain-wide activity during *C. elegans* mating. *Cell* **184**, 5122-5137 (2021).
- 903 55. D. R. Albrecht, C. I. Bargmann, High-content behavioral analysis of *Caenorhabditis*
904 *elegans* in precise spatiotemporal chemical environments. *Nat. Methods* **8**, 599-605
905 (2011).

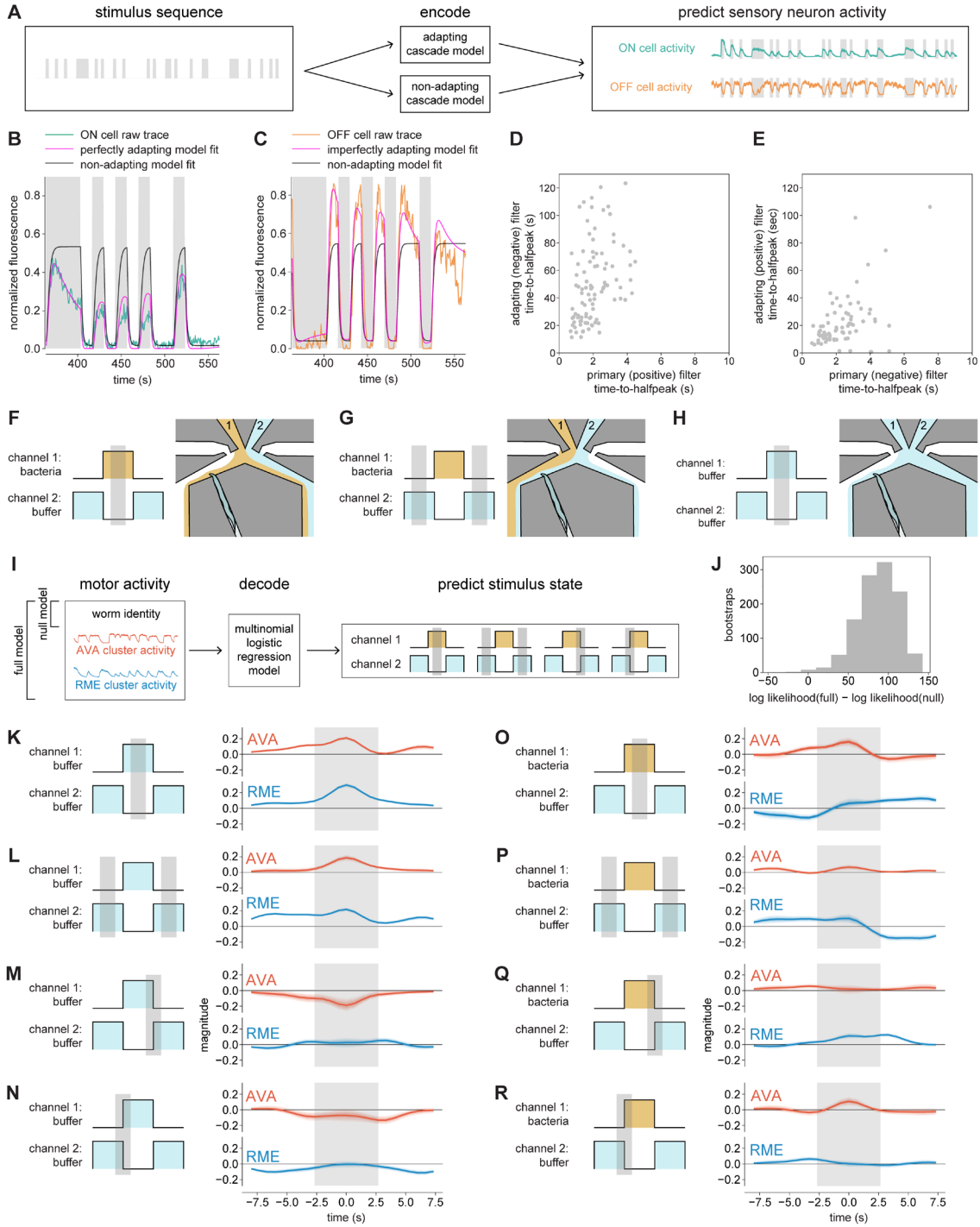
- 906 56. E. A. Pnevmatikakis, A. Giovannucci, NoRMCorre: An online algorithm for piecewise rigid
907 motion correction of calcium imaging data. *J Neurosci Methods*. **291**, 83-94 (2017).
908 57. D. A. Fish, A. M. Brinicombe, E. R. Pike, J. G. Walker, Blind deconvolution by means of
909 the Richardson–Lucy algorithm. *JOSA A* **12**, 58-65 (1995).
910 58. L. Paninski, J. Pillow, J. Lewi, Statistical models for neural encoding, decoding, and
911 optimal stimulus design. *Prog Brain Res*. **165**, 493-507 (2007).
912 59. D. Bates, M. Mächler, B. Bolker, S. Walker, Fitting linear mixed-effects models using
913 lme4. *arXiv [Preprint]* (2014). <https://arxiv.org/abs/1406.5823> (accessed 31 October
914 2021).

915 **Figures and Tables**
916



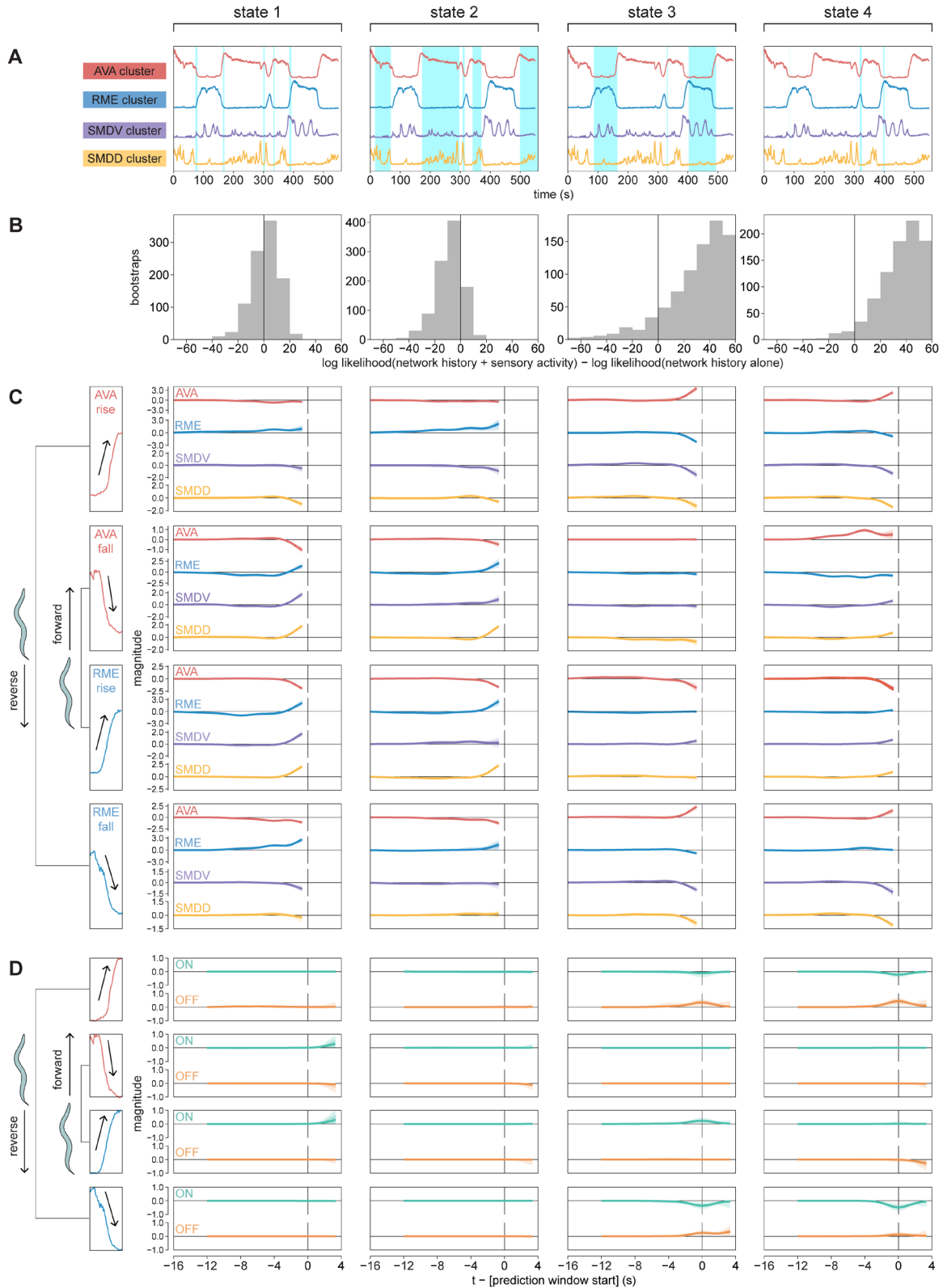
918

919 **Figure 1.** Food-stimulated whole-brain activity reveals six functional clusters. (A) Stimulus
920 presentation and imaging setup. A computer precisely controls delivery of a stimulus sequence
921 that alternates between variable-length pulses of two liquid flows: bacterial food stimulus (gold)
922 and control buffer (light blue). This stimulus sequence is presented to the nose of a *C. elegans*
923 animal that is restrained in a microfluidic chip. Volumes of the *C. elegans* head are acquired and
924 subsequently processed to acquire calcium traces. (B–D) Identification of neurons in the
925 NeuroPAL–GCaMP6s strain. Some photobleaching occurred due to acquisition after calcium
926 imaging (see Methods: Cell Identification). (B) RME motor neuron and AVA command neuron. (C)
927 SMDD motor neuron. (D) SMDV motor neuron. (E) Neurons and their associated direction of
928 locomotion. (F–G) Number of neurons in each functional cluster for all animals, based on > 85%
929 correlation with representative neurons. (F) non-NeuroPAL–GCaMP5K animals. (G) NeuroPAL–
930 GCaMP6s animals. (H) Calcium activity of low-noise active neurons for a single worm. Gray
931 shading represents bacterial stimulus pulse duration. (I–K) Calcium activity averaged across all
932 traces within a functional cluster. Colors of average calcium traces corresponds with colors of
933 individual traces in (H). (I) OFF and ON clusters. (J) AVA and RME clusters. (K) SMDD and
934 SMDV clusters.
935



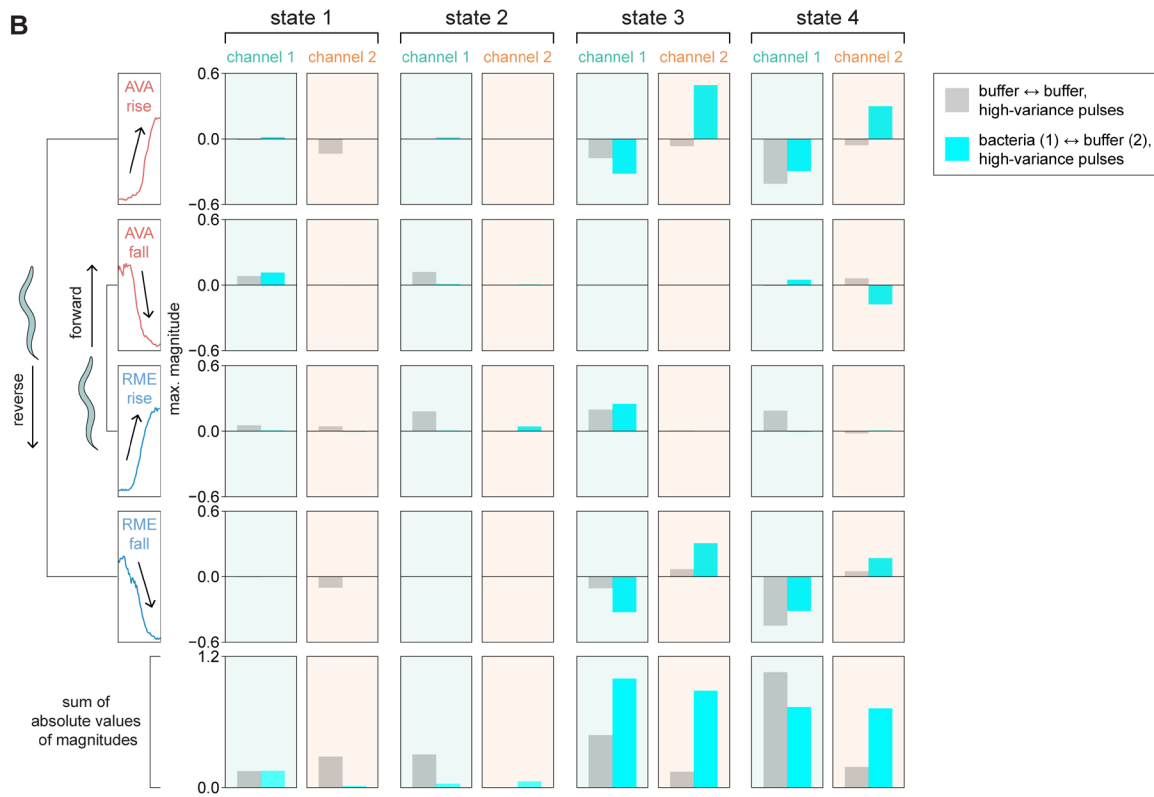
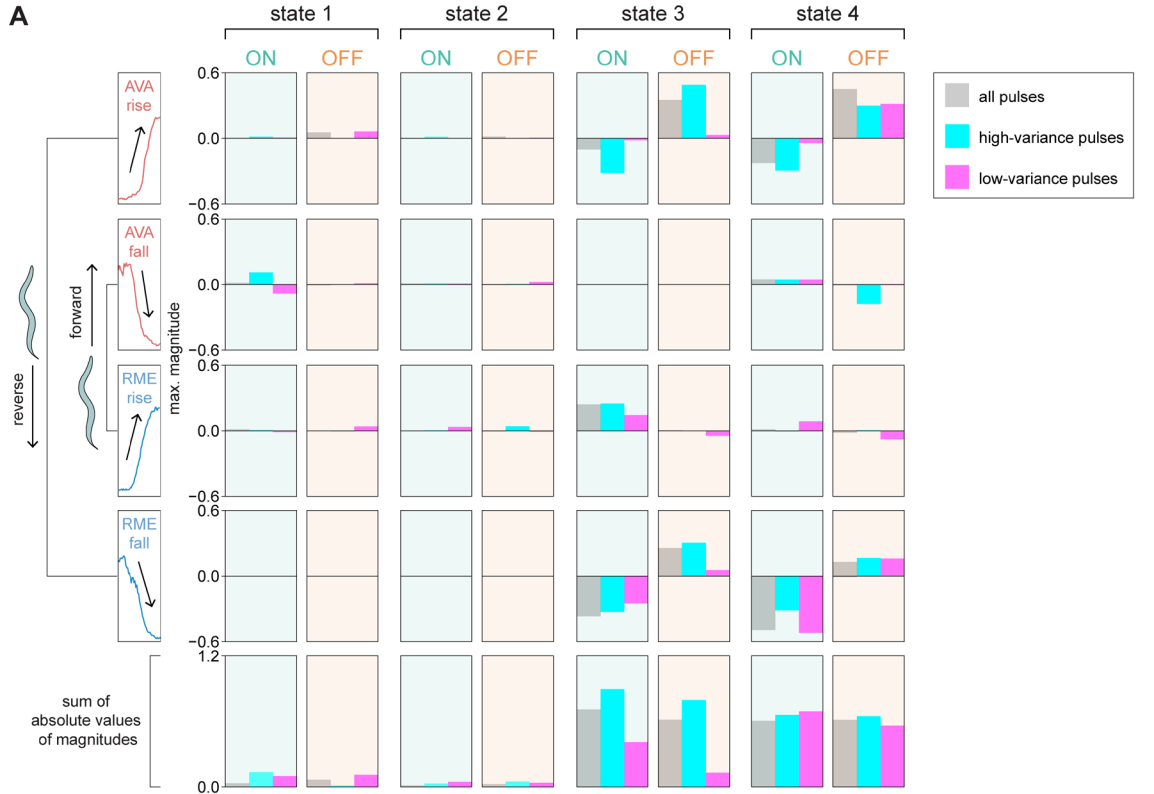
937
938

939 **Figure 2.** Bacteria onset and removal differentially drive activity of sensory, AVA, and RME
940 clusters. (A) Stimulus sequence features are fed into an encoding model (see Materials and
941 Methods: Encoding model) to predict sensory cluster activity. (B–C) Representative examples of
942 sensory neurons raw traces compared with model predictions. (B) ON cell. (C) OFF cell. (D–E)
943 Time-to-half-peak distributions for the best performing (D) ON and (E) OFF cell adapting models.
944 (F–H) Stimulus states (left, highlighted in gray) and their corresponding flow configurations
945 relative to the *C. elegans* nose. (F) Bacteria from channel 1 flows over nose. (G) Buffer from
946 channel 2 flows over nose. (H) As a control, buffer emanates from both channel 1 and channel 2.
947 (I) AVA and RME cluster activity, as well as worm identity, is fed into a decoding model (see
948 Materials and Methods: Decoding model) to predict different stimulus states (highlighted in gray).
949 In the null model, only worm identity is used. (J) Out-of-bootstrap cross-validation performance of
950 the full decoding model that includes AVA and RME cluster activity. (K–R) Temporal filters
951 predicting stimulus states from AVA and RME cluster activity for buffer↔buffer stimulus
952 sequences (K–N) and bacteria↔buffer sequences (O–R). Gray shading represents the prediction
953 time window (with 0 s as the halfway point of the prediction window), such that preceding time
954 represents baseline activity and subsequent time represents delayed effects. Median bootstrap
955 temporal filters are plotted, with graded shading indicating 50%, 75%, and 90% of bootstraps.
956
957

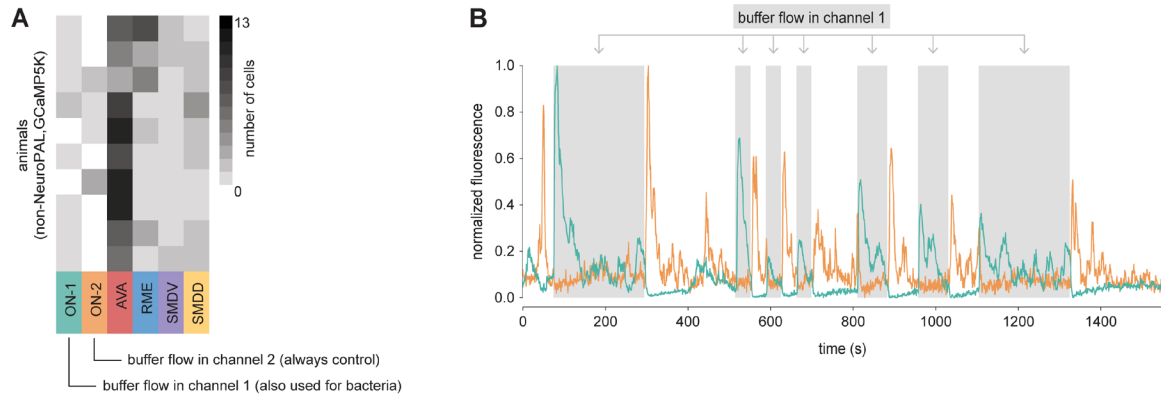


959
960

961 **Figure 3.** Identification of interpretable network states that vary in sensory gating properties. (A)
962 The top four network states identified by the soft decision tree gating model portion of the SDT-
963 MLR forecasting model (see Fig. S5, Materials and Methods: SDT-MLR model). Cyan shading
964 represents the time windows for which a particular state's probability exceeds 0.75. (B–C)
965 Temporal filters predicting rise and fall of AVA and RME cluster activity from (B) recent history of
966 AVA, RME, SMDV, and SMDD cluster motor/command activity; and (C) ON and OFF cell cluster
967 sensory activity. (B–C) Median bootstrap temporal filters are plotted, with graded shading
968 indicating 50%, 75%, and 90% of bootstraps. (D) Difference in out-of-bootstrap cross-validation
969 performance between models that included both network history and sensory activity and models
970 that that only included network history.
971

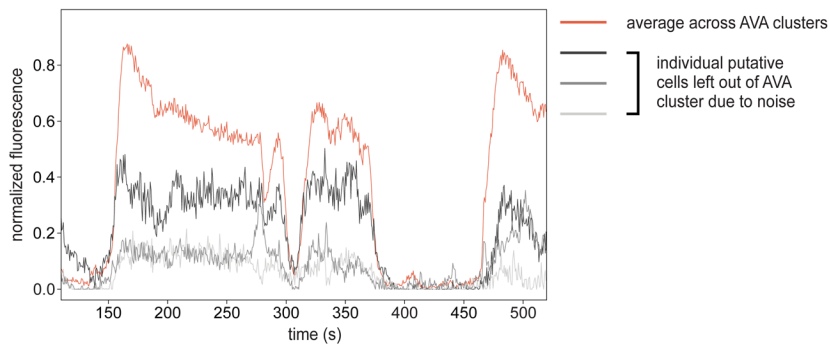


974 **Figure 4.** Effect of stimulus timescales and sensory context on AVA and RME clusters. (A–B)
975 Maximum magnitudes of temporal filters predicting rise and fall of AVA and RME activity from
976 sensory neuron clusters. Maximum magnitudes are calculated from $t-12s$ to $t-0s$ relative to the
977 start of the prediction window (t). Sums of absolute values of magnitudes measure the overall
978 sensory influence within a state. (A) Comparison of all stimulus pulse lengths, only high-variance
979 pulses, and only low-variance pulses. (B) Comparison of buffer↔buffer and bacteria↔buffer
980 stimulus sequences. Only high-variance pulses were compared. Channel 1 and 2 are the same
981 as ON and OFF, respectively, for bacteria↔buffer stimulus sequences, as seen in (A).
982



984

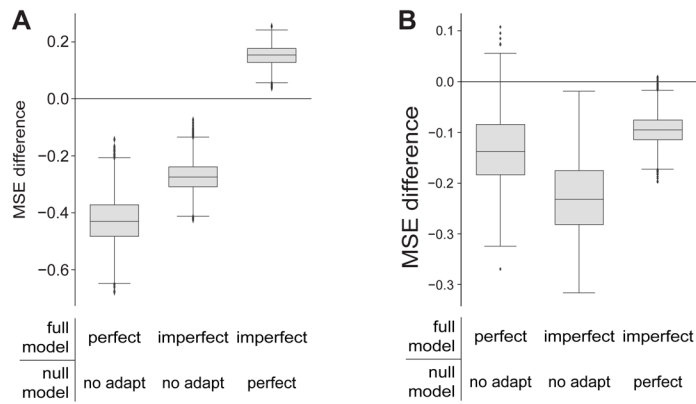
985 **Figure S1.** Characteristics of functional clusters in animals presented with buffer↔buffer stimulus
986 sequences. (A) Number of neurons in each functional cluster. (B) Example traces of ON-1 (green)
987 sensory neurons that respond to buffer from channel 1, and of ON-2 (orange) sensory neurons
988 that respond to buffer from channel 2.
989



991
992
993
994
995
996

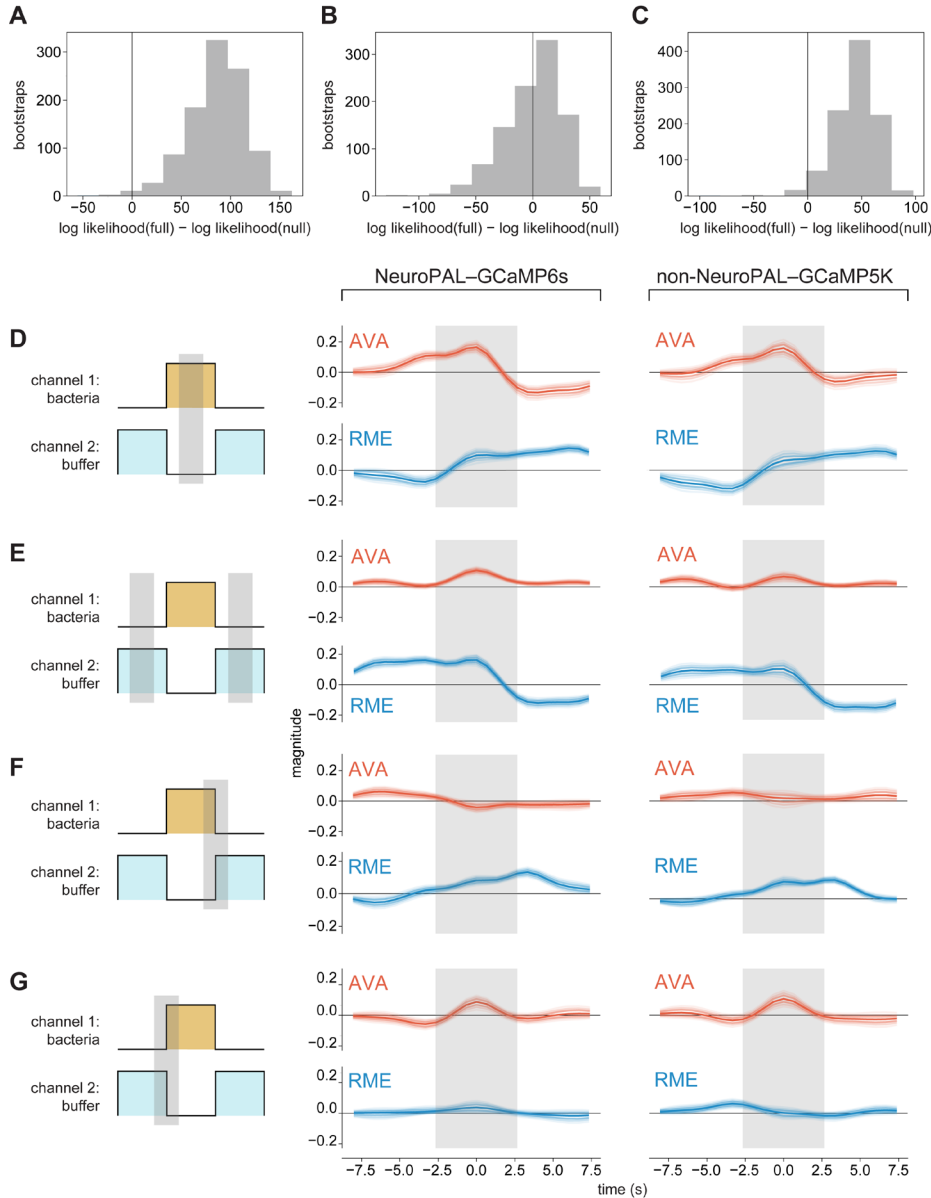
Figure S2. High-noise neuronal traces omitted from clusters still exhibit similarity to cluster activity. Non-sensory neurons that did not exhibit strong correlation (>85%) with AVA, RME, SMDD, or SMDV were excluded from clusters. Examples of excluded high-noise cells that resemble the AVA cluster are shown.

997



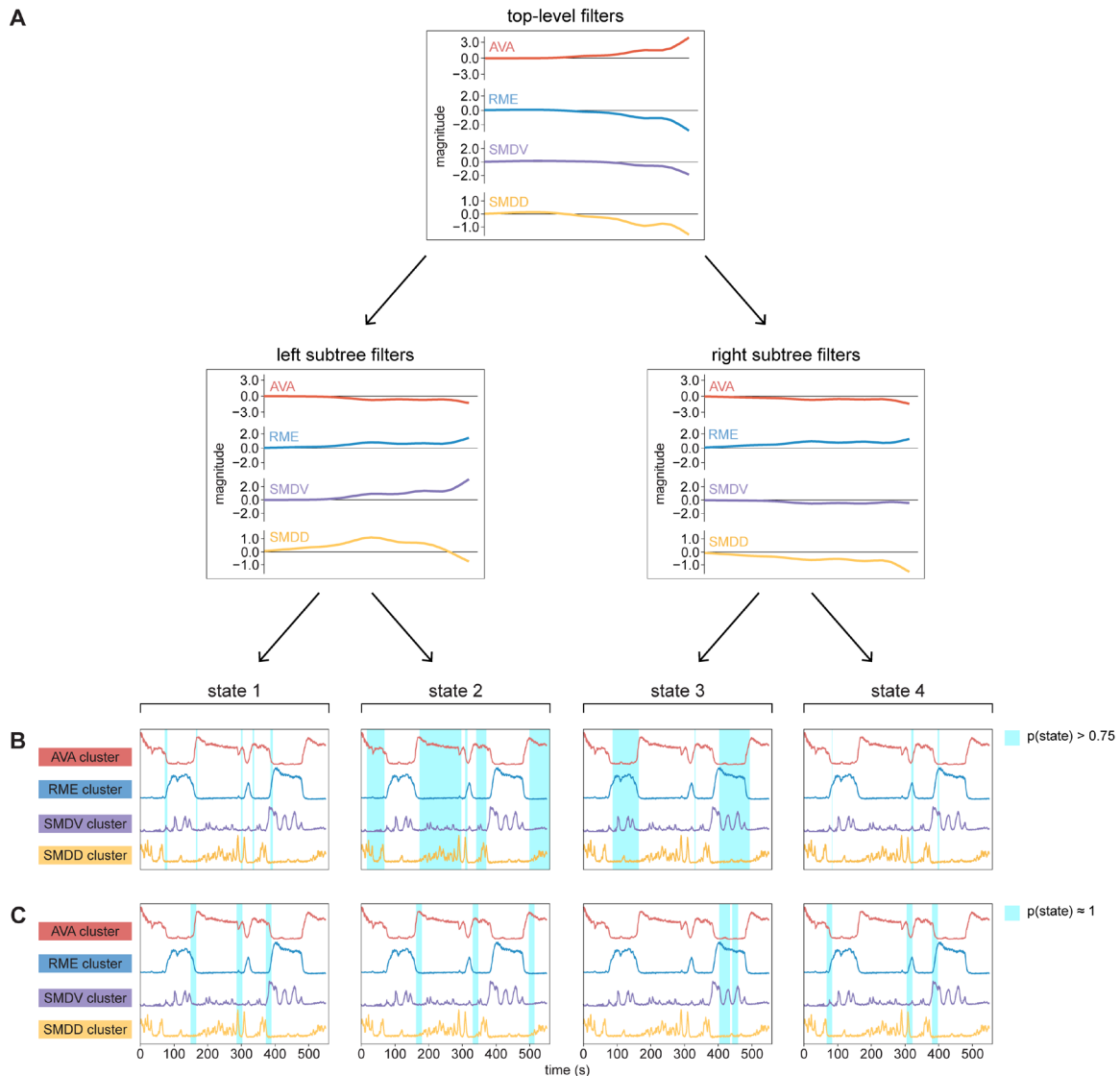
999

1000 **Figure S3.** Encoding model performance. Performance comparison of (A) ON and (B) OFF cell
1001 models with varied levels of adaptation, as measured by the change in MSE (mean squared
1002 error) from the null model to the full model. Boxplots represent the distribution of MSE differences
1003 across hierarchical bootstraps.



1005 **Figure S4.** AVA and RME activity from both NeuroPAL-GCaMP6s and non-NeuroPAL-
 1006 GCaMP5K strains are similarly driven by bacterial stimuli. (A–C) Out-of-bootstrap cross-
 1007 validation model performance for the full decoding model that includes (A) AVA and RME cluster
 1008 activity from the NeuroPal-GCaMP6s strain during bacteria↔buffer stimulus sequences, (B)
 1009 SMDD and SMDV cluster activity from the non-NeuroPal-GCaMP5K strain during
 1010 bacteria↔buffer stimulus sequences, and (C) AVA and RME cluster activity from the non-
 1011 NeuroPal-GCaMP5K strain during buffer↔buffer stimulus sequences. (D–G) Temporal filters
 1012 predicting stimulus states from AVA and RME cluster activity, for NeuroPAL-GCaMP6s (left) and
 1013 non-NeuroPAL-GCaMP5K (right) strains. Gray shading represents prediction time windows,
 1014 such that preceding time represents baseline activity and subsequent time represents delayed
 1015 effects. Median bootstrap linear filters are plotted, with graded shading indicating 50%, 75%, and
 1016 90% of bootstraps. (B) prolonged bacteria, (C) prolonged buffer, (D) bacteria-to-buffer transition,
 1017 and (E) buffer-to-bacteria transition.

1018



1020

1021

1022

1023

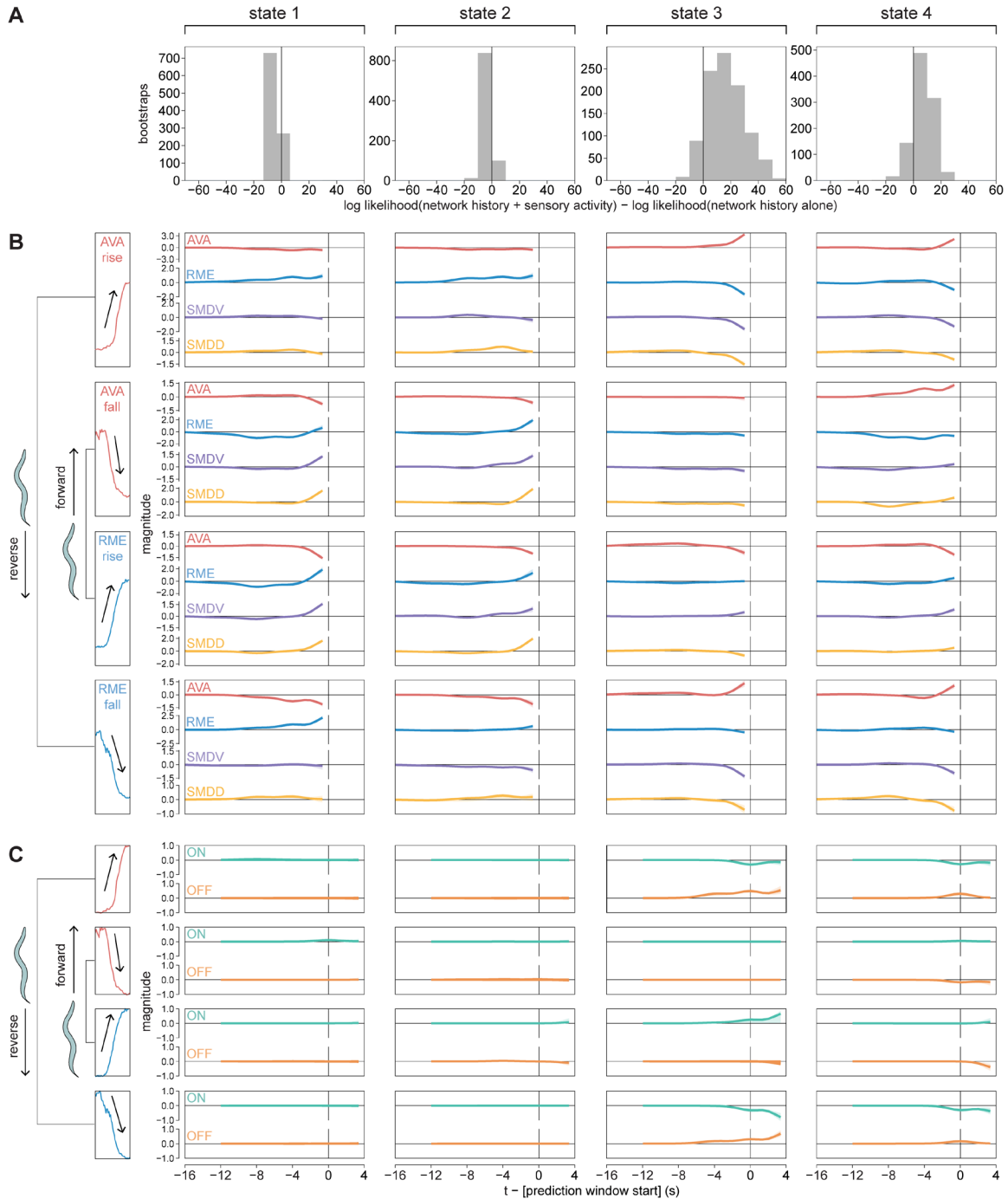
1024

1025

1026

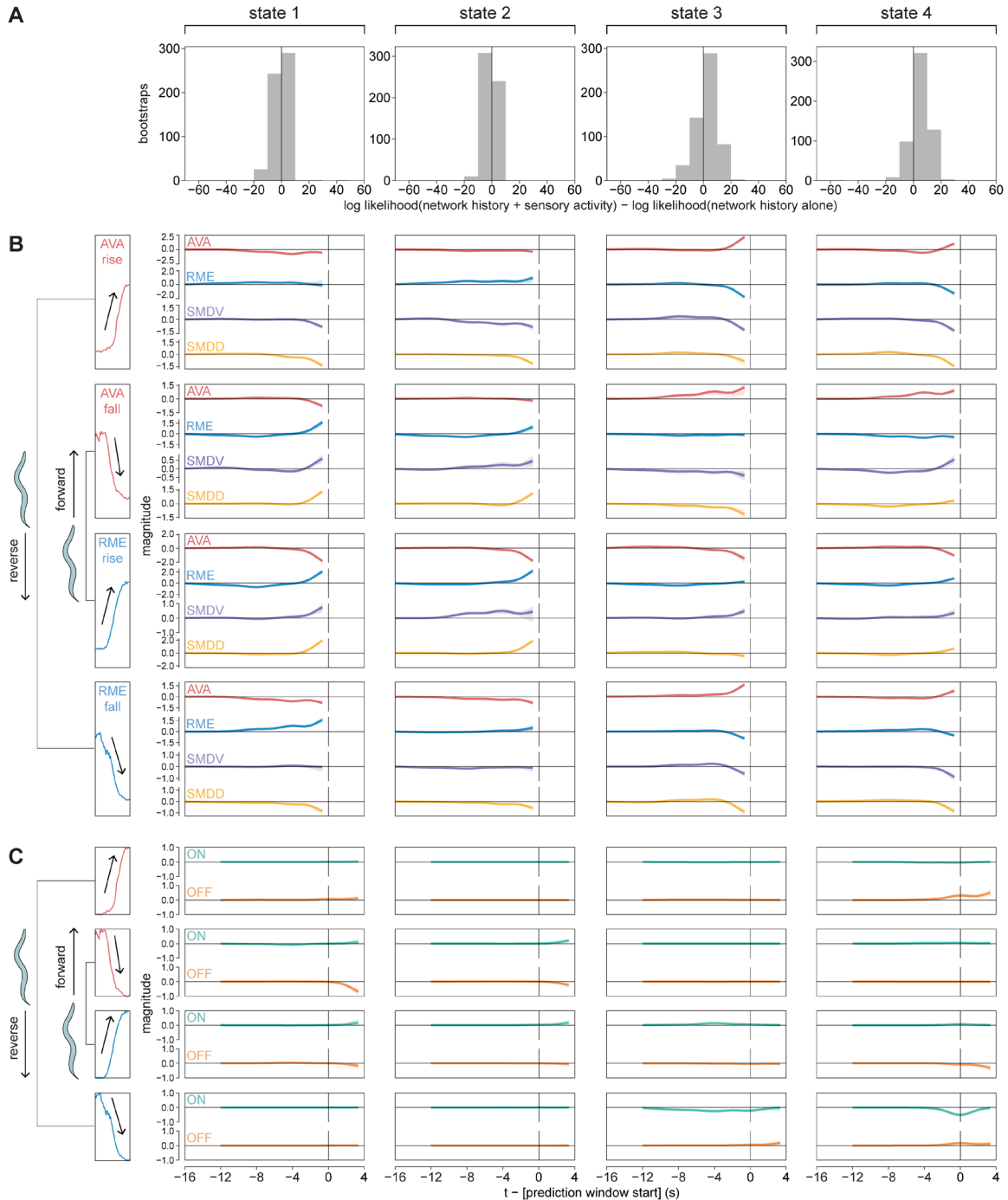
1027

Figure S5. Tree organization of SDT-MLR model. (A) Hierarchical filters divide the space of network trajectories into different linearizable subspaces. (B) The top four network states identified by the soft decision tree gating model portion of the SDT-MLR forecasting model (same as Fig. 3A). Cyan shading represents the time windows for which a particular state's probability exceeds 0.75. (C) Time was binned into windows, from which state-maximizing windows, in which $p(\text{state}) \approx 1$, were selected to be used as input for MLR submodels.

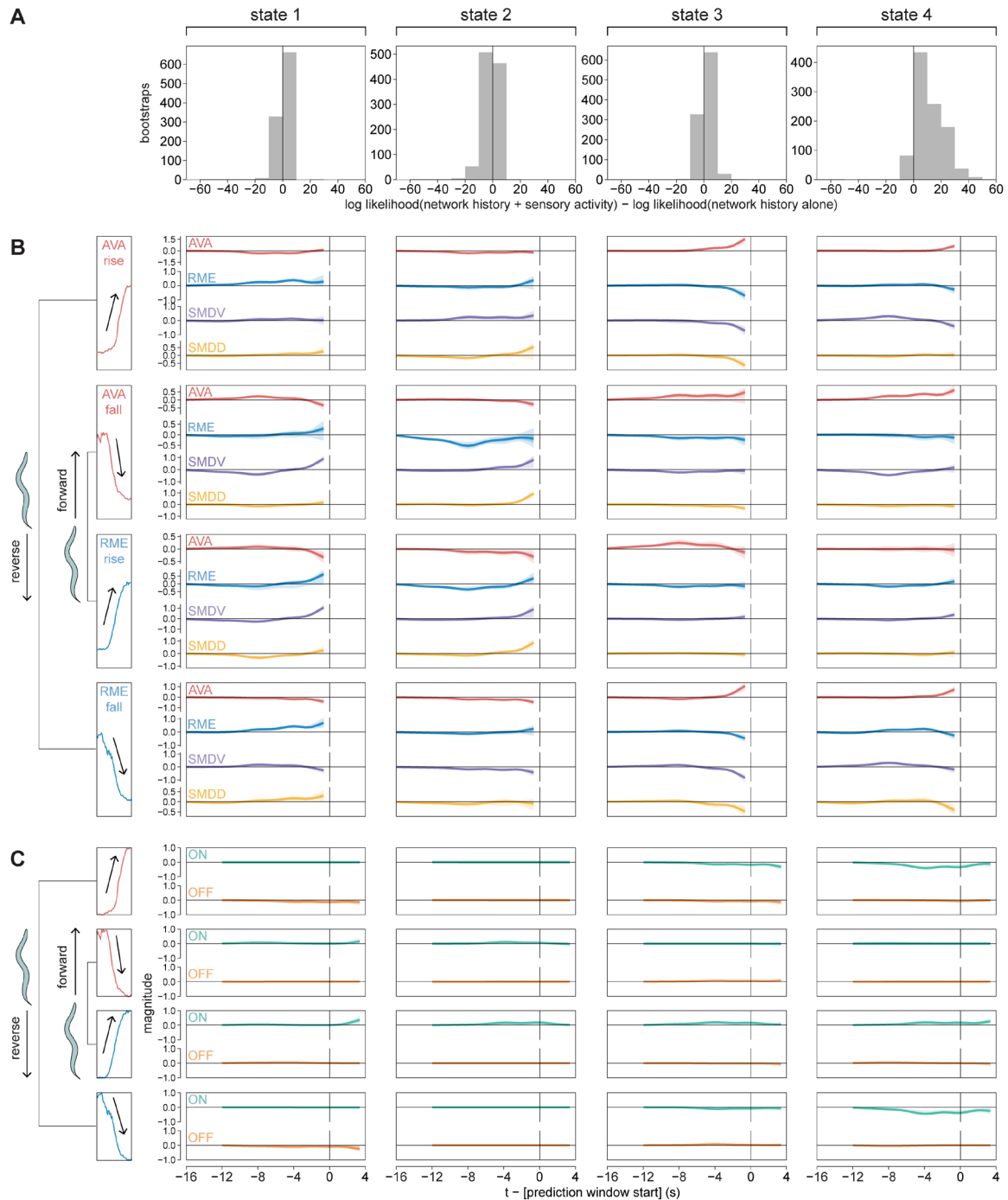


1029

1030 **Figure S6.** SDT-MLR model with only high-variance pulses from bacteria↔buffer stimulus
 1031 sequence presentation. (A) Difference in out-of-bootstrap cross-validation performance between
 1032 models that included both network history and sensory activity and models that that only included
 1033 network history. (B–C) Temporal filters predicting rise and fall of AVA and RME cluster activity
 1034 from (B) recent history of AVA, RME, SMDV, and SMDD cluster activity; and (C) ON and OFF cell
 1035 cluster sensory activity. (B–C) Median bootstrap temporal filters are plotted, with graded shading
 1036 indicating 50%, 75%, and 90% of bootstraps.



1038
 1039 **Figure S7.** SDT-MLR model with only low-variance pulses from bacteria↔buffer stimulus
 1040 sequence presentation. (A) Difference in out-of-bootstrap cross-validation performance between
 1041 models that included both network history and sensory activity and models that that only included
 1042 network history. (B–C) Temporal filters predicting rise and fall of AVA and RME cluster activity
 1043 from (B) recent history of AVA, RME, SMDV, and SMDD cluster activity; and (C) ON and OFF cell
 1044 cluster sensory activity. (B–C) Median bootstrap linear filters are plotted, with graded shading
 1045 indicating 50%, 75%, and 90% of bootstraps.



1047

1048

1049 **Figure S8.** SDT-MLR model for buffer↔buffer stimulus sequence presentation, high-variance

1050 pulses only. (A) Difference in out-of-bootstrap cross-validation performance between models that

1051 included both network history and sensory activity and models that that only included network

1052 history. (B–C) Temporal filters predicting rise and fall of AVA and RME cluster activity from (B)

1053 recent history of AVA, RME, SMDV, and SMDD cluster activity; and (C) ON and OFF cell cluster

1054 sensory activity. (B–C) Median bootstrap temporal filters are plotted, with graded shading